Article:
Zuccarini, A., Vasu, N.N., Banks, V.J. et al. (2025) PIV analysis of flow-type landslides under suboptimal image conditions. Landslides, 22 (7). pp. 2413-2432. ISSN: 1612-510X

https://doi.org/10.1007/s10346-025-02498-8

Title: PIV analysis of flow-type landslides under suboptimal image conditions

Zuccarini A.[1*], *Vasu N.N.*[2], *Banks V.J.*[2], *Bowman E.T.*[3], *Leonardi A.*[3], *Berti M.*[1]

[1]Department of Biological, Geological, and Environmental Sciences (BiGeA), University of Bologna, via Zamboni 67, Bologna, Italy

[2] British Geological Survey, Nicker Hill, Keyworth, Nottingham NG12 5GG, UK

[3] Department of Civil and Structural Engineering, University of Sheffield, Sheffield, UK

*Corresponding author
email: alessandrozuccarini27@gmail.com
full postal address: Via Zamboni, 67 - 40126 Bologna

Abstract

The dynamics of flow-type landslides, including earthflows and debris flows, is still not fully understood, primarily due to the complexity of the physical processes that govern the flow and the challenges in acquiring direct field measurements. In modern monitoring stations, cameras represent cost-effective data sources, providing essential information for characterising documented reactivation events. *Particle Image Velocimetry (PIV)* algorithms have been extensively employed in the literature to reconstruct velocity fields and rheological behaviour of laboratory physical models under ideal conditions. However, the resolution of camera footage in the field typically falls short of being optimal due to lighting and weather conditions, as well as non-zenithal recording geometry, hindering a straightforward application of *PIV*. This study presents two primary sets of laboratory flume tests conducted to explore a broad range of recording conditions, bridging the gap between ideal laboratory settings and actual field acquisitions. The experiments enabled the evaluation of *PIV* performance for each image quality scenario, detailing and quantifying the main uncertainties as well as their impact on the resulting velocity fields while discussing underlying reasons and mitigation measures. The experimental results reveal that, with due adjustments, suboptimal-quality footage can be used to estimate the actual flow velocity field and infer the rheological behaviour of the flow. Furthermore, distortions related to non-zenithal perspectives can be reliably minimised through suitable orthorectification algorithms. These findings support the potential for broader application of the tested *PIV*-based methodological approach in field scenarios to investigate the dynamics of flow-type landslides.

Keywords: Flume experiments, Particle Image Velocimetry (PIV), flow velocity field, flow-type landslides

Declaration of Competing Interest

The authors declare no conflict of interest.

Acknowledgements

This study was carried out within the RETURN Extended Partnership and received funding from the European Union Next-GenerationEU (National Recovery and Resilience Plan – NRRP, Mission 4, Component 2, Investment 1.3 – D.D. 1243 2/8/2022, PE0000005.

Authors' contribution statements

Conceptualisation: Matteo Berti and Alessandro Zuccarini; *Data collection and material preparation*: Alessandro Zuccarini, Nikhil Nedumpallile Vasu, Vanessa J. Banks, Elisabeth T. Bowman and Alessandro Leonardi; *Methodology*: Matteo Berti and Alessandro Zuccarini; *Formal analysis and investigation*: Alessandro Zuccarini and Matteo Berti; *Writing - original draft preparation*: Alessandro Zuccarini; *Writing - review and editing*: Matteo Berti, Nikhil Nedumpallile Vasu, Vanessa J. Banks, Elisabeth T. Bowman and Alessandro Leonardi; *Funding acquisition*: Matteo Berti; *Resources*: Matteo Berti; *Supervision*: Matteo Berti. All authors read and approved the final manuscript.

1. Introduction

The dynamics and mechanisms underlying the behaviour of flow-type landslides kinematics are still subject to debate and not fully understood in the literature, encompassing both faster debris flows (Kaitna et al. 2016; Nagl et al. 2020) and slower earthflows (Picarelli et al. 2005; Carrière et al. 2018; Berti et al. 2022). This knowledge gap primarily stems from the complexities of the processes and from the difficulties in acquiring direct field measurements (Hürlimann et al. 2003; McArdell et al. 2007), as well as in replicating these phenomena through representative laboratory-scaled physical models (Iverson 2015; Turnbull et al. 2015). Modern monitoring stations frequently employ a variety of sensors to investigate flow dynamics, including geophones (Mainsant 2012; Walter 2017; Coviello et al. 2019), infrasound sensors (Leng et al. 2017), pore water pressure transducers and load cells (Hürlimann et al. 2019), typically coupled with video cameras to document the events. Field cameras, in particular, represent a cost-effective and highly valuable tool for data collection, providing essential information to characterise captured flow-type landslides. When flow depth is known, surface velocity observations enable the reconstruction of the transverse distribution of the depth-averaged shear rate. This, in turn, allows at least a qualitative inference of the rheological properties of the flow.

Image-based analysis techniques, such as *Particle Image Velocimetry* (*PIV*) and *Particle Tracking Velocimetry* (*PTV*), have been extensively reported in the literature to accurately reconstruct internal and surface deformation and velocity fields, and to investigate the rheological behaviour of physical models under ideal and controlled laboratory conditions (e.g. GDR MiDi 2004; Faug et al. 2015). Over the past 30 years, *PIV* algorithms have also been frequently applied to larger scales, referred to as *Large-Scale Particle Image Velocimetry (LSPIV)*, particularly in hydraulic applications to analyse the surface velocity distribution of rivers and evaluate their discharge (e.g. Fujita et al. 1998; Le Coz et al. 2010; Gunawan et al. 2012; Muste et al. 2014). More recently, *LSPIV* has also been employed to estimate the surface velocity of debris flows (e.g. Theule et al. 2018). In particular, Schöffl et al. (2023) combined *LSPV*-derived surface velocity measurements with contextual Pulse-Doppler high-frequency radar observations, while Aaron et al. (2023) and Spielmann & Aaron (2024) proposed a novel approach utilising high-frequency 3D *LiDAR* (Light Detection And Ranging) point clouds as an alternative to conventional camera recordings for *LSPIV* analysis.

The determination of the surface velocity distribution through the implementation of these methods with adequate spatial resolution would allow the assessment of flow boundary conditions. Integrating information from qualitative observations on the recorded footage and independent morphological assessments enables inference of the rheological behaviour of the landslide material. However, since *PIV* outcomes are highly dependent on input footage quality (Prasad et al. 1992), its transposition to

larger-scale field scenarios and processes is not straightforward. Factors such as adverse weather conditions or inadequate and inconsistent lighting can significantly impact the quality of the acquired images. Physical barriers, including fog, dust or raindrops, may distort captured footage by scattering light or causing uneven focus, resulting in a blurred effect. Furthermore, due to frequently limited accessibility and difficult setup conditions in the field, cameras are often placed at a non-zenithal perspective on the channel and non-optimal recording distances. This potentially introduces severe distortions in the acquired footage, leading to the reconstruction of velocity values and distributions that are not representative of the flowing landslide mass. Additionally, image quality may be further impacted by motion blur, which occurs when the frame rate of the installed cameras, especially in the context of low-cost monitoring stations, is not sufficient to fully capture the movement of the flow.

In this study, two sets of flume experiments were conducted to test the applicability of *PIV* algorithms under different input image quality conditions, from ideal laboratory acquisitions to suboptimal recordings that mimic typical field footage. The main objective is to assess *PIV*'s ability to produce reliable flow field data using blurred images and non-zenithal recording angles and to identify uncertainties arising from these suboptimal conditions.

Section 2 outlines the experimental setup and the analysis workflow adopted. Section 3 presents the main experimental results, while Section 4 explores the main sources of uncertainties in the techniques employed, considering their application in the field.

2. Methods

2.1 Experimental setup

Figure 1a schematically illustrates the experimental setup employed in the two sets of landslide flume experiments, referred to as *F1* and *F2*, conducted at the Department of Civil and Structural Engineering at the University of Sheffield (Figure 1b) and the British Geological Survey site in Keyworth (Figure 1c), respectively. Both series of tests focused on observing dry granular flows from different perspectives as they were gradually released from the flume hopper. The selection of dry granular materials was driven by the need to design straightforward experimental setups, prioritising data acquisition and processing over the precise replication of in situ phenomena in terms of material properties and scaling. Despite the similarity of the processes observed, the recording conditions in the two sets of experiments, summarised in Table 1, were systematically different, as detailed in the following sections.

132 *2.1.1 F1 tests*

133 The *F1* tests featured recordings from two optimal perspectives utilising a high-performance high-
134 speed camera, sharply capturing dry granular flows of approximately 3.85 mm Denstone® ceramic
135 beads (Zhao et al. 2023) at 1000 frames per second (fps). The first recording geometry (R_1) positioned
136 the camera above, facing the chute surface perpendicularly to capture the flow from an ideal *zenithal*
137 perspective. The second viewing angle involved positioning the camera perpendicularly to the side
138 of the flume, recording the side of the flow through the smooth Perspex wall and aligning with the
139 fixed chute's slope (θ) at 30° from the horizontal. This ideal perspective, while not accessible in the
140 field, is commonly utilised in flume experiments to investigate internal flow dynamics (e.g.
141 Wiederseiner et al. 2011; Li et al. 2022).
142 These acquisition geometries were established to frame fixed regions on both the surface and side of
143 the chute, as indicated by the green and blue squares in Figure 1a, respectively. This setup enabled
144 consistent recording and characterisation of surface and internal velocity distributions within the same
145 portion of the flow. Cameras were positioned to focus on regions around the flume's midpoint, aiming
146 to capture as uniform flow as possible and minimise potential effects from the material release at the
147 upper slope or the transition to free-fall motion near the chute's end.
148 To facilitate the generation of a regular flow, potentially reaching a steady-state condition over time,
149 upon which to focus the analyses, the granular material was progressively released from the flume
150 hopper through a sluice gate, avoiding *dam-break* release mechanisms, typically employed in debris
151 flow physical models (e.g. Iverson et al. 2010; Eu et al. 2017). The initial thickness of the flow (h_0)
152 and the material's release rate were controlled by the gate opening (H) and the material's head in the
153 hopper, which gradually decreased during the experiment. Care was taken to maximise the initial
154 head while maintaining an even distribution of the material within the hopper, ensuring a uniform
155 release rate throughout a significant portion of the test.
156 With a single high-speed camera available, each flow was repeatedly captured from different
157 recording geometries, while maintaining consistent boundary and initial conditions. Subsequently,
158 the boundary conditions at the chute's base were systematically altered to increase surface roughness,
159 documenting eventual variations in the flow dynamics. The transparent Perspex sidewalls were
160 consistently kept unchanged to ensure continuous observation. As detailed in Table 1, three main
161 tests have been conducted: one employing the standard smooth aluminium base, another with an
162 intermediate roughness base composed of glued ceramic beads of about 1 mm diameter, and a third
163 using a coarse sand base with particle sizes ranging from 1 to 2 mm.
164 Unlike similar experiments described in the literature, which often include a seeding phase, where
165 coloured, fluorescent or reflective tracer particles are added to the material to enhance flow patterns

(Savage 1979; Parsons et al. 2001; Lindken 2009), the tests performed omitted this procedure. The texture of the granular materials employed was deemed adequate to enable the reconstruction of flow dynamics, given proper lighting. This was achieved using 50W DC LED floodlights (Figure 1b).

2.1.2 F2 tests

In contrast to the *F1* experiments, which involved the application of the *PIV* algorithm to sharp footage captured from optimal recording angles, the *F2* experiments explored different acquisition geometries and image quality scenarios. In addition to the ideal perspectives (R_1 and R_3) used in the *F1* experiment set, the *F2* tests implemented an additional recording geometry ($R2$). This other observation angle involved positioning the camera slightly to the side of the flume, facing downslope with an inclination of 20° relative to the flume slope (θ), capturing the surface of the flow from a more oblique, non-zenithal perspective (Figures 1c and 3). This suboptimal camera orientation mirrors the recording geometry typically employed in the field, where achieving a perfectly zenithal perspective can be challenging (Patalano et al. 2017). In the field, cameras are commonly placed to the side of the channel, slightly inclined downward to minimise interference from rain droplets and at a generally low angle relative to the horizontal.

The *F2* experiments featured simultaneous recordings of the same region of the flume from the three described perspectives of dry granular flows composed of fine sand ($d_{mean} \approx 0.28$ mm), utilising regular cameras with maximum frame rates of 240 fps. Multiple tests were conducted at progressively higher flume slope angles (θ) while maintaining the other boundary conditions constant. This approach resulted in increasingly faster flows and, given the fixed camera frame rate, gradually blurrier and lower-quality footage, enabling the consideration of a wide spectrum of image quality conditions.

Despite these methodological differences, the *F2* tests were conducted with the same care and precautions as detailed for the *F1* experiments, specifically regarding material preparation and release, as well as camera positioning around the mid-portion of the flume length, ensuring the recording of flows as regular and uniform as possible.

As with the *F1* experiments, the *F2* tests were performed under the assumption that no seeding phase was needed, contributing to the generation of challenging conditions for the application of the *PIV* algorithm to suboptimal quality footage (see Section 3.2). Nevertheless, this setup is representative of field conditions, where seeding is not possible. Similar to *F1* tests, lighting was provided using multiple 50W DC LED floodlights (Figure 1c).

2.2 Analysis workflow

Despite the slight differences in experimental procedures between the two described sets of tests, the acquired footage was processed following the same analysis workflow schematised in Figure 2.

2.2.1 The PIV algorithm

PIV algorithms are non-intrusive optical measurement techniques used to determine the velocity field of recorded fluid flows. This is achieved by identifying the displacement of similar groups of pixels (or particles) in successive images through cross-correlation methods (Adrian 1991). The captured frames are initially subdivided into a grid of smaller sub-regions, framed by a moving interrogation window, or *patch*, whose size and shift define the final measurement resolution. For each consecutive image pair, the cross-correlation matrix is evaluated within the moving interrogation patch. The location of resulting cross-correlation peaks provides the most probable displacement vectors, connecting the similar groups of pixels identified between the two consecutive frames along a straight line (Raffel et al. 2007; Thielicke and Stamhuis 2014). This information, combined with the timestep between images, ultimately yields the frame-by-frame flow velocity field. Unlike Lagrangian *PTV* techniques, which reconstruct the trajectory of individual tracer particles (Kreizer et al. 2010), *PIV* algorithms are Eulerian methods that enable the reconstruction of the flow vectors regardless of single particle characteristics (Patalano et al. 2017).

For both the *F1* and *F2* experiments, a *PIV* analysis was conducted on the frames extracted from the footage recorded from the different perspectives based on the camera's frame rate, employing the open-source algorithm *PIVlab* (Thielicke and Stamhuis 2014). This particular algorithm utilises a multi-pass approach, where each flow vector results from successive computational steps during which the original moving interrogation patch is progressively deformed and refined. The first step involves computing the frame-by-frame displacement vectors between similar groups of pixels by evaluating two-dimensional cross-correlation peaks within a moving interrogation patch (Thielicke and Sonntag 2021), following the described basic *PIV* principles. In the subsequent step, the displacement information obtained within the first interrogation patch is interpolated for every enclosed pixel and used to deform the second-pass patch. Within this finer patch, the cross-correlation matrix peaks are evaluated by repeating the procedure followed in the previous pass, thereby refining the input displacement information. Through this iterative process, the algorithm yields progressively more accurate and refined displacement vectors, enhancing correlation robustness and decreasing random error contributions (Thielicke 2014).

234 *2.2.2 Optimal images*

235 In the flume experiments performed in this study, a two-pass *PIV* approach was adopted in the *PIVlab*
236 environment defining interrogation patch sequences of 64x64 – 32x32 pixels and 24x24 – 12x12
237 pixels, for *F1* and *F2* tests, respectively. The interrogation patch size, especially for *F1* experiments
238 where larger particles were employed, was defined to enclose around 5 – 15 particles on average to
239 improve correlation significance (Adrian and Westerweel 2011; Gollin et al. 2017). Additionally, the
240 interrogation patch shift in the moving window algorithm was consistently set to 50% of its size.
241 Consequently, as depicted in Figure 2a, for each pair of extracted frames, the two-dimensional flow
242 displacement and corresponding velocity fields were derived, with a flow vector density determined
243 by the size and shift of the moving patch. The obtained velocity fields, initially expressed in
244 pixels/frame, were converted to real units (m/s) by defining the time step between frames and the
245 pixel size. The latter was determined by calibrating the images against known distances: the chute
246 width for the surface velocity field and a reference distance measured on a ruler taped to the flume
247 sidewall within the camera's field of view for R_3 recordings.
248 After retrieving the frame-by-frame velocity field, the analysis focused on a specific subset where the
249 flow exhibited steady-state behaviour. This approach facilitated more meaningful comparisons
250 between recordings acquired from different geometries, whether obtained in separate tests (*F1*) or
251 simultaneously (*F2*). The extraction of the steady-state frames subset was performed as follows. First,
252 two section traces were defined perpendicular to the flow direction, bounding the edges of an ideal
253 plane transversally crossing both the surface and the side of the flume at the same distance from the
254 hopper, applicable to the R_1 and R_3 recording geometries, respectively. Along these traces, for R_1
255 acquisitions, a short section, indicated as *Section (I)* and represented by a red solid line in Figure 2a,
256 was traced around the mid portion of the chute to capture the central part of the flow surface.
257 Similarly, another short section, limited to the upper portion of the flow, was considered for R_3
258 footage. Subsequently, for each recording geometry, the frame-by-frame mean velocity value along
259 the defined sections was computed and observed over time, as illustrated in the chart in Figure 2b.
260 The subset of frames exhibiting an overall constant mean velocity, indicated by a null slope of the
261 regression line and suggesting steady-state flow conditions, was isolated and extracted, while the
262 preceding frames were discarded. The steady-state surface and side velocity profiles were then
263 extracted for the selected frame subset along the same sections, but this time considering the entire
264 extent of the flow, as indicated by the red dashed line in Figure 2a for R_1 recordings, labelled as
265 *Section (II)*. The resulting velocity profiles, along with their mean distribution resampled at regular
266 intervals, and the corresponding standard deviation values were ultimately plotted as shown in Figure
267 2c to summarise the steady-state surface and internal velocity distributions of the recorded flow. For

validation, the reconstructed velocity values were compared with manually derived measurements obtained by visually tracking frame-by-frame individual particle trajectories at multiple flow depths on the same steady-state subset of R_3 recordings. These independent velocity measurements were taken using a ruler affixed to the side of the flume and visible within the camera's field of view.

2.2.3 Suboptimal images

The methodological approach detailed in the previous section for analysing sharp footage from ideal perspectives in both experiment sets was also applied to suboptimal images, with minor modifications. Specifically, the analysis workflow remained unchanged for the blurred footage captured in the *F2* experiments from the ideal perspectives, whereas it was properly adjusted for R_2 acquisitions regardless of image quality. While pixel size is uniform across the image for R_1 and R_3 acquisitions, this is not the case for R_2. In such instances, the non-zenithal recording angle introduces a significant disproportion between pixel sizes in the foreground and background. Background pixels are generally more poorly resolved, with differences and gradients depending on the geometric relationship between the captured portion of the channel and the camera, both in terms of recording angle and distance (Jolley et al. 2021).

Consequently, converting and transposing the pixel reference system of the images to real coordinates and units is not as straightforward as with R_1 and R_3 recordings. Applying the same methodology could result in significant deviations of the reconstructed flow velocities from the actual values. Therefore, to assess the contribution and remove such optical distortions, the obtained R_2 surface velocity field (Figure 3a) was appropriately orthorectified using the open-source algorithm *RIVeR* (Patalano et al. 2017). This software enables orthorectification operations directly on *PIV*-derived flow velocity fields within a user-defined two-dimensional region of interest. This is accomplished by computing the homography matrix (Corke 2011), which uniquely maps real-world coordinates to their planar projection on the image within the selected area. This matrix is solved using the *Camera Calibration Toolbox* (Vision Caltech 2009) for MATLAB by specifying the real-world and image coordinates of a series of known control points (Figure 3b). While four control points are sufficient to perform 2D orthorectification, solving the homography matrix in three dimensions requires the spatial coordinates of at least six points. Given the controlled conditions of the present experiments, which focused on steady-state flows over flat and regularly shaped chutes, the simpler 2D orthorectification approach using four control points was deemed adequate. However, as noted in Section 4.3, more complex field scenarios may necessitate 3D orthorectification to account for irregular geometries and unsteady flow conditions.

The calculated homography matrix is then utilised to extend the image-to-real-world coordinate system relationship to the entire region of interest, accurately determining the actual pixel size (Figure 3c) and reprojecting the flow velocity vectors as if derived from a zenithal observation (Figure 3d). The resulting R_2 orthorectified velocity profiles were ultimately compared and plotted against the corresponding uncorrected ones and those derived from the zenithal perspective (R_1), which ideally represent the actual surface velocity distribution of the flow.

Despite the existence of advanced techniques for mitigating motion blur and restoring image sharpness, including deconvolution algorithms (Lucy 1974; Hosseini & Plataniotis 2020; Satish et al. 2020) and more sophisticated machine learning approaches (Zhang et al. 2017; Lian & Wang 2023; Chen 2024), the described methodology was applied directly to the unprocessed camera footage, prioritising operational simplicity and straightforward implementation for future field applications.

3. Results

This section presents the results obtained from the *F1* (Section 3.1) and *F2* (Section 3.2) laboratory flume tests, conducted employing the experimental setup and processing procedures detailed in Section 2.

3.1 *F1* tests

Figure 4 summarises the results of the three main flume experiments in the *F1* set, comparing the mean velocity profiles and corresponding standard deviation bands of the steady-state flows recorded from R_1 (Figure 4a) and R_3 (Figure 4c) perspectives, under the three varying boundary conditions at the base of the flow indicated in Table 1. The velocity profiles reconstructed for the flows with the smooth aluminium, intermediate roughness (1 mm ceramic beads), and coarse angular sand beds are displayed in blue, green, and red, respectively. The blue curves exhibit the highest velocities, with values of approximately 1.7 m/s around the central region and 1.5 m/s towards the shallower portions of the flow in the surface and side velocity distributions, respectively. Conversely, the green and particularly the red curves consistently display lower velocities, with mean values of 1.6 m/s and 1.3 m/s, and 1.2 m/s and 0.7 m/s, respectively, evaluated in the same regions of the flow. These curves not only highlight a significant overall velocity reduction with increasing chute surface roughness but also display a consistent marked continuity between surface and side velocity distributions, revealing comparable values at the intersections between the analysed section pairs.

Examining the side velocity profiles (Figure 4c), the employed sluice gate opening (H) of 85 mm, corresponding to a flow thickness normalised by particle size ratio (h/d) of approximately 22, resulted in varying flow thicknesses across the different bed types. The angular sand bed produced the thickest

flows, measuring around 38 mm, while values of 27 and 24 mm were documented for the smooth and intermediate roughness bases, respectively. In terms of normalised *h/d* ratios, these values correspond to approximately 10, 7 and 6.

Additionally, the side velocity profiles reveal progressively different flow conditions as bed roughness increases and overall flow velocity decreases. The faster flows over smooth and intermediate roughness beds share similar velocity distributions, with progressively lower values with depth that remain visibly above zero at the bottom, indicating a *slip-flow* rheological behaviour (Nagl et al. 2020). In contrast, the high-roughness bed produces distinct flow conditions, characterised by a steeply decreasing velocity profile, reaching zero at the base. This particular rheological behaviour, alternatively referred to as *heap flow* (GDR MiDi 2004; Jop et al. 2005, 2006), where the flow is concentrated in the upper portions, marks the transition from inclined plane flow to flow on an erodible bed. Within this flow, the grains effectively move over a lower, thinner *quasi-static* layer (Jop 2015) of interlocked particles due to the base roughness.

The distinct rheological behaviours observed are also quantitatively highlighted by the velocity coefficient α, computed as the ratio between the depth-averaged velocity along the vertical investigated in the proximity of the transparent sidewall and the corresponding surface velocity. Flows over smooth and intermediate roughness bases, exhibiting similar rheological behaviour, reveal comparable α values of 0.73 and 0.68, respectively, aligning with the 0.6 – 0.8 range reported in the literature for flows in dense granular media (Cui et al. 2018; Nagl et al. 2020; Aaron et al. 2023; Spielmann & Aaron 2024). In contrast, flow conditions over the rough sand base yield a remarkably lower α value of 0.34.

Although this rheological behaviour transition is remarkable in the side profiles, the corresponding surface ones (Figure 4a), net of the overall varying velocities, do not reflect any indication of the documented changes in internal flow conditions. This is further highlighted in the normalised profiles displayed in Figure 4b, with velocity distributions consistently collapsing onto a common trend, making it virtually impossible to infer the actual rheological behaviour and internal flow structure from surface observations alone. This complexity, common in flume experiments, arises from systematically different boundary conditions at the bottom and the side of the flow, framed by a progressively rougher base and smooth Perspex walls, resulting in undifferentiated slip-flow conditions along the sides.

Overall, *F1* tests indicate the effectiveness of the *PIV* technique in characterising flows under optimal conditions. This is evidenced by the consistent agreement between *PIV*-derived velocity and independent manual measurements performed at four distinct flow depths, which systematically fall within the standard deviation bands of the mean steady-state profiles displayed in Figure 4c. The low

standard deviation values relative to the mean enable the proper identification of the flow velocity profiles. Notably, the quality of the reconstructed side velocity distributions allows for the observation of varying flow regimes, which align with the expected behaviour of the flow under the defined boundary conditions.

3.2 *F2* tests

Figure 5 summarises the results from *F2* experiments testing and assessing the applicability of the described *PIV* methodology under varying input image quality conditions. Among the various experiments performed, two reference cases are presented, depicting ideal and sub-optimal acquisition conditions within the spectrum of recording scenarios explored. These configurations are represented by the blue and red curves in the figure, corresponding to slower flows with a slope angle (θ) of 28° and faster ones with θ = 30°, respectively. As illustrated by the frames in Figure 5a, for a fixed camera frame rate, increasingly faster flows due to higher slope angles (θ) translate into progressively poorer image quality, transitioning from ideal, sharp images to blurrier frames. Similar to Figure 4 for the *F1* experiments, the curves displayed represent the mean velocity distributions along with the corresponding standard deviation values of the steady-state flows recorded from the R_1 (Figure 5a) and R_3 (Figure 5b) camera geometries. Apart from a consistently greater dispersion around the mean values for the blurrier footage, the curves reveal that the applied methodology can coherently reproduce the flow, estimating velocity distributions in both scenarios. This is further corroborated by the positive correspondence with independent, visually determined velocities at three different flow depths, which consistently align with and fall within the standard deviation values of the R_3 profiles shown in Figure 5b. Despite the different flow velocities, the two sets of curves exhibit similar distributions with *slip-flow* behaviour at the interfaces with the smooth aluminium base and Perspex walls, consistent with the rheological behaviour expected for a dry granular flow governed by the described boundary conditions. The observed similarity in flow conditions is further supported by the numerical values of the velocity coefficient (α), calculated consistently with the *F1* experiment set. The tests conducted at $\theta = 28°$ and $\theta = 30°$ yield analogous α values of 0.83 and 0.81, respectively, both comparable with the previously reported literature range of 0.6 – 0.8 for such phenomena.

The side velocity profiles in Figure 5b reveal slight differences in flow thickness. With an initial gate opening (H) of 40 mm ($h/d \approx 143$), thicker flows of about 10.5 mm were observed at θ = 30°, while slightly lower values around 9.5 mm were observed at θ = 28°. These thicknesses correspond to normalised h/d ratios of approximately 34 and 38, respectively.

Additionally, as highlighted in the *F1* tests, the velocity profiles in Figure 5 display a systematic continuity between the surface and side velocity fields, with values of approximately 0.1 m/s and 0.3

m/s documented for $\theta = 28°$ and $\theta = 30°$ flows, respectively, near the intersection of the analysis sections.

Figure 6 condenses the results of the *F2* tests focused on evaluating the effects of a *non-zenithal* recording geometry (R_2) on reconstructing the surface velocity distribution of the flow compared to its actual velocity field, ideally determined from a zenithal perspective (R_1). The R_1 surface velocity profiles reconstructed for the flows observed at $\theta = 28°$ and $\theta = 30°$, described in Figure 5a, are reported as green curves in Figures 6a and 6b, respectively. In both figures, the blue profiles represent the surface velocity distributions obtained for the same flows from recording geometry R_2, where pixel size was considered homogeneous across the entire image and defined uniquely based on a known distance coinciding with the chute width. These curves, for which input image distortion was not corrected, significantly and systematically underestimate the real flow velocity distribution, with an average offset of approximately 55% for $\theta = 28°$ and 65% for $\theta = 30°$. Conversely, a consistent alignment with the real surface velocity distribution is documented in both scenarios for the orthorectified R_2 profiles, depicted in red in Figures 6a and 6b, exhibiting comparable offsets of about 2% on average. This highlights that sub-optimal quality footage from non-zenithal recording geometries can be effectively employed for estimating the surface velocity field of a flow when appropriate orthorectification algorithms are applied.

4. Discussion

4.1 Effects of suboptimal image quality

The results from the *F2* flume tests revealed that the methodological approach employed enables a reasonable estimate of flow velocity fields even under suboptimal image quality conditions (Section 3.2). However, to consistently assess and quantify the effects of image blur on the *PIV*-derived velocity distributions, the *F2* experimental footage captured at $\theta = 28°$ from the zenithal perspective (R_1) was considered. The quality of the original sharp footage was progressively artificially decreased by applying a *Gaussian smoothing* algorithm. *Gaussian smoothing* is a two-dimensional convolution operation that utilises a moving kernel represented by a Gaussian function to transform the enclosed original image pixels, reducing their noise and detail, and resulting in blurred images (Marr and Hildreth 1980; Shapiro and Stockman 2001). The blur level is controlled by the standard deviation (σ) of the Gaussian distribution employed. A wide spectrum of image blur scenarios was considered, using values of σ ranging from 1 to 5. For each σ, the mean surface velocity profile was reconstructed along the same section and compared to the original.

The mean velocity profiles obtained reveal a consistent increase in uncertainty with σ, with standard deviation values 20% higher than the original for $\sigma = 1$, and up to 2 or 5 times the original for $\sigma = 3$

and σ = 5, respectively. Additionally, as displayed in Figure 7a, the shape of the original velocity distribution reported in green is gradually less recognisable transitioning to higher blur levels. Besides the greater uncertainty, these velocity profiles consistently and sensibly underestimate the original values, up to an average difference of approximately 45 % for σ = 5. This bias is attributable to the poorer quality of the input images, which results in broader and less distinct peaks in the cross-correlation matrix evaluated in the *PIV* algorithm, leading to a decrease in the signal-to-noise ratio, and, consequently, reduced correlation accuracy (Elsinga et al. 2005). This causes the generation of spurious velocity vectors that do not accurately represent the recorded flow. These vectors exhibit orientations that can significantly deviate from the actual flow direction, as displayed qualitatively in the plan view (Figures 7b, c) and quantitatively along a reference section (Figures 7d, e) for the same frames pair under optimal and blurred (σ = 5) image quality conditions. While in the former case, the flow vectors are uniformly oriented at about 90° relative to the analysis section, they become more chaotic for σ = 5, revealing diverging orientations characterised by peak differences of approximately ± 60°, indicating fictitious transversal velocity components. These transversal components may lead to a substantial reduction in the velocity magnitude values extracted along the reference section, thereby motivating the consistent velocity underestimation observed.

As synthetically shown in Figure 7 and further detailed in Figures 8 and 9 in the supplementary materials, the effect of image blur may be partially mitigated by defining a sequence of larger interrogation patches in the *PIV* analysis. For instance, Figure 7 highlights how the adoption of an interrogation window sequence of 96 – 48 pixels, four times larger than the 24 – 12 pixels patches used in the initial analysis, produces a clear reduction in uncertainty and underestimation of the flow velocity as σ increases, albeit with a reduced spatial resolution. In this case, for σ = 5, the deviation of the velocity distribution from the original values, indicated by the red and green dashed curves in Figure 7a, respectively, decreases from approximately 45% to 20%. Additionally, the distribution of the velocity vector orientations along the analysis section, depicted by the black dashed curves in Figures 7d and 7e, more closely aligns with the original, with deviations consistently below ± 10° from the true flow direction.

While the usage of larger interrogation windows visibly enhances *PIV* analysis results for suboptimal-quality footage, with the improvement proportional to the level of image blur, the effect is less pronounced for sharp images. Maximum differences of approximately 2% were observed between the velocity profiles reconstructed from sharp frames employing interrogation patch sequences of 24 – 12 pixels and 96 – 48 pixels, depicted by the two green curves in Figure 7a.

The fact that the accurate reconstruction of flow dynamics is not hampered when individual particles within the flow are not clearly recognisable, provided the discussed adjustments are applied, supports the reasonable extension of the adopted methodology to the analysis of more complex multiphase flows in both laboratory and field settings.

4.2 Effects of inadequate frame rate

Another crucial parameter in field acquisitions, particularly in the context of low-cost monitoring systems, is the recording camera's frame rate. To investigate the impact of inadequate sampling frequency on flow velocity field reconstruction, the *F2* experimental footage captured at $\theta = 28°$ from the zenithal perspective (R_1) was again used as a reference. The original 240 fps footage was progressively undersampled down to 30 fps, with *PIV* analysis performed at each intermediate step to compare the reconstructed surface velocity distributions.

The resulting mean velocity profiles reveal a marked increase in uncertainty towards lower frame rates. Standard deviation values were 20% higher than the original at 120 fps, and up to 2 and 4 times higher at 60 fps and 30 fps, respectively. Similar to the motion blur effect described in the previous section, Figure 10 illustrates how the shape of the original velocity distribution (reported in green) becomes less recognisable towards lower frame rates, consistently underestimating velocity values. This discrepancy stems from the reduced temporal resolution in the undersampled footage, where actual particle displacements exceed the size and shift of the *PIV* moving interrogation window. This aliasing effect leads to a systematic loss of correlation between frame pairs (Raffel et al. 2007), generating biased flow velocity vectors that inaccurately reflect the observed flow. These spurious vectors display orientations that diverge remarkably from the true flow direction, as shown qualitatively from a zenithal perspective in Figures 10b and 10c, and numerically along a reference section in Figures 10d and 10e, for the same image pairs captured at the original and reduced (30 fps) frame rates. While properly sampled footage, produces a homogeneously oriented velocity field at about 90° relative to the analysis section, undersampled recordings exhibit a more chaotic distribution of vectors, with some even directed upstream and orientation deviations of up to ± 120° from the actual direction.

Figure 10 also briefly illustrates that undersampling effects can be effectively mitigated by adopting larger interrogation patch sequences during *PIV* analysis. Specifically, employing a window sequence of 96 – 48 pixels, four times larger than the original, leads to a sharp reduction in uncertainty and underestimation of flow velocity at lower frame rates, albeit at the cost of a coarser spatial resolution. For example, at 30 fps, the velocity deviation from the original values drops approximately from 80% to 1%. Similarly, the velocity vector orientations along the analysis section, highlighted by the black

dashed curves in Figures 10d and 10e, closely align with the original, with deviations consistently under ± 2° from the true flow direction.

The effects of using larger interrogation windows are further illustrated in Figures 11 and 12 in the supplementary materials, concerning patch sequences of 48 – 24 pixels and 94 – 48 pixels, respectively.

4.3 Orthorectification uncertainties

The methodological approach adopted in the *F2* experiments highlighted that the use of appropriate orthorectification algorithms on the *PIV*-derived surface velocity field can mitigate distortions introduced by non-zenithal recording geometries (R_2). The two-dimensional orthorectification algorithm employed requires specifying the coordinates of four known control points, framing an ideal plane where the transposition between the pixel reference system and the real-world coordinates is performed based on the actual size of the pixels enclosed. While defining these control points as well as their respective distances in a controlled, small-scale laboratory environment is straightforward, in the field, these operations may present a more significant challenge depending on the accessibility of the landslide channel. This could lead to inaccuracies in determining these distances and, consequently, in estimating the actual flow velocity field.

To assess and quantify the potential effects of measurement errors on the final surface velocity distribution, the orthorectification procedure was repeated on the same footage captured at $\theta = 28°$ multiple times, artificially modifying the control points' distance values. The real distances were progressively altered considering errors of ± 5%, 10% and 15%. The resulting velocity profiles are compared in Figure 13. Overestimations of the actual distances result in profiles that increasingly overestimate both the channel width and flow velocity, whereas underestimations yield the opposite effect. These deviations are represented in the figure by curves grading from green (actual values) to red (overestimation) or blue (underestimation). The displayed distributions reveal that, in our experiments, the input percentage error in the distances approximately corresponds to the deviation observed with respect to the real velocity profile, both positively and negatively.

In addition to evaluating uniformly distributed errors across the region of interest, the potential effect of measurement errors affecting a single control point was also considered. Artificially altering the inter-distances associated with one control point, simulating its misidentification in the field, produced a pronounced distortion of the orthorectified velocity field towards the modified point. This resulted in surface velocity profiles that not only exhibited different flow widths but also displayed markedly asymmetric trends, deviating from the original distribution with an intensity proportional to the error magnitude. The abnormal shape of these velocity distributions, characterised by values progressively increasing towards one side of the channel, could serve as an indicator in field

538 applications, suggesting the presence of errors concentrated on the identification of a single control
539 point.
540 Given the potential significance of such errors, it is crucial in the field to measure the channel
541 geometry within the field of view of the monitoring camera as accurately as possible.
542 In natural environments, challenges in orthorectification extend beyond the discussed complex
543 channel geometries, which may hinder the uniform distribution of control points and compromise
544 their precise positioning. Further complexities arise from the transient nature of the observed
545 phenomena. While the flume experiments described in this study focused on steady-state flows with
546 constant thickness and velocity, such stable conditions are rarely encountered in real-world scenarios.
547 Under fluctuating flow levels, the recording distance between the camera and the flowing mass
548 becomes variable, and pronounced changes can significantly alter the area encompassed within the
549 region of interest identified for *PIV* analysis and orthorectification procedures. These fluctuations
550 complicate the accurate mapping of real-world coordinates into the 2D image plane where the flow
551 velocity field is reconstructed (Li et al. 2019). For instance, flow level underestimation leads to
552 exaggerated horizontal distances and, in turn, velocity overestimation, while flow level
553 overestimation produces opposite effects (Dramais et al. 2011). Consequently, flow level variability
554 represents a primary source of uncertainty in *LSPIV* analyses (Le Boursicaud et al. 2016).
555 Recent literature shows that *LSPIV* has predominantly been applied in riverine environments (Muste
556 et al. 2008; Zhu & Lipeme Kouyi 2019). Studies indicate that 2D orthorectification algorithms,
557 similar to those employed in the flume tests described, are suitable for relatively narrow channels
558 (approximately 10 – 20 m wide) with regular geometries, where the four specified control points and
559 flowing water can be reasonably assumed to lie within the same plane (Patalano et al. 2017; Bodart
560 et al. 2024). Conversely, in cases involving more complex channel geometries, irregular riverbank
561 topographies, or fluctuating flow levels, more advanced 3D orthorectification algorithms are
562 generally required (Le Coz et al. 2010; Detert 2021). These methods typically necessitate identifying
563 at least six control points, preferably up to ten for redundancy and better reliability (Fujita and Kunita
564 2011; Jolley et al. 2021), distributed uniformly along the observed channel segment. Notably, simply
565 increasing the number of control points does not inherently reduce orthorectification uncertainty.
566 Rather, the precision in locating these points is critical, making fewer but highly accurate control
567 points generally preferable to a larger number with less precise measurements (Le Coz et al. 2021;
568 Bodart et al. 2024).
569 Episodic flow-like landslides, such as debris flows, typically exhibit transitions between a front, a
570 central body, and a tail, potentially grading into hyperconcentrated water flows (Turnbull et al. 2015).
571 These events may feature successive surges, resulting in significant flow depth variations up to

several meters (Zanuttigh & Lamberti 2007; Meyrat et al. 2022). Therefore, adopting 3D orthorectification algorithms is essential for field applications. Additionally, segmenting the acquired footage into subsets based on homogeneous flow levels can help mitigate orthorectification uncertainty caused by fluctuating flow depths (Theule et al. 2018).

Further laboratory flume tests would be required to thoroughly investigate and quantify errors and limitations of the orthorectification process, particularly as a function of the non-zenithal (R_2) camera placement. This would involve systematically varying the viewing angle, recording distance, and potentially the flow level, enabling a comprehensive understanding of how these factors impact the accuracy of reconstructed velocity fields.

5. Conclusions

In this study, two sets of laboratory flume experiments were performed between the Department of Civil and Structural Engineering at the University of Sheffield (*F1*) and the British Geological Survey site in Keyworth (*F2*). The primary goal was to assess *PIV* algorithm capabilities across a range of recording scenarios, from ideal laboratory settings to suboptimal conditions typical of field observations, and validate a methodology that could be employed to reconstruct the surface velocity distribution of flow-type landslides and acquire insights into their rheological behaviour.
Based on the research findings, the following conclusions can be drawn:

1) The experiments performed under optimal conditions demonstrate the efficacy of the *PIV* algorithm in reconstructing the velocity distributions of observed flows. Additionally, the processing of tests monitored using zenithal and lateral cameras emphasises the critical role of understanding the boundary conditions at the base and sides of the flow to reasonably estimate its rheological behaviour. This is particularly crucial in field applications, especially if attempts are made to infer the internal dynamics of the flow based on the exclusively available surface velocity distribution.

2) Non-zenithal footage, commonly available from field acquisitions, can be effectively utilised to retrieve the real surface velocity distribution of the flow by adopting appropriate orthorectification techniques. The analyses underscore the importance of accurately defining suitable control points in the field for the orthorectification algorithm, noting that percentage errors in measuring their inter-distances result in comparable deviations in the reconstructed velocity profiles.

3) Footage from widely deployed low-cost field camera monitoring systems, often characterised by blurriness, suboptimal quality, or insufficient sampling rates, can still be used to estimate the surface velocity distribution of flows, albeit with non-negligible uncertainty. This uncertainty may include

significant underestimations of the actual flow velocity, which can be detected and reasonably mitigated by adopting sequences of larger interrogation patches in the *PIV* analysis, at the cost of slightly lower spatial resolution.

The present work establishes the foundation for applying the detailed and tested methodological framework to the in-depth characterisation of field-recorded debris flow events, addressing both rheological behaviour and hydrodynamic parameters. A comprehensive analysis is currently underway, including rigorous comparisons with field observations and numerical modelling analyses, which will be presented in a forthcoming study.

6. References

Aaron J, Spielmann R, McArdell BW, Graf C, 2023. High-frequency 3D LiDAR measurements of a debris flow: A novel method to investigate the dynamics of full-scale events in the field. Geophysical Research Letters, 50. https://doi.org/10.1029/2022GL102373.

Adrian RJ, 1991. Particle-imaging techniques for experimental fluid mechanics, Annual Review of Fluid Mechanics, 23, p. 261 – 304. http://dx.doi.org/10.1146/annurev.fl.23.010191.001401.

Adrian RJ, Westerweel J, 2011. Particle Image Velocimetry. Cambridge University Press, Cambridge. ISBN: 978-0-521-44008-0.

Berti M, Castellaro S, Zuccarini A, 2022. Field measurements, laboratory tests and empirical relations for investigating the solid-to-fluid transition of a rapid earthflow, Engineering Geology, 296. https://doi.org/10.1016/j.enggeo.2021.106486.

Carrière SR, Jongmans D, Chambon G, Bièvre G, Lanson B, Bertello L, Berti M, Jaboyedoff M, Malet JP, Chambers JE, 2018. Rheological properties of clayey soils originating from flow-like landslides, Landslides 15(8), p. 1615 – 1630. https://doi.org/10.1007/s10346-018-0972-6.

Chen L, Zhang J, Li Z, Wei Y, Fang F, Ren J, Pan J, 2024. Deep Richardson–Lucy Deconvolution for Low-Light Image Deblurring. International Journal of Computer Vision 132(2), p. 428 – 445. https://doi.org/10.1007/s11263-023-01877-9.

Corke P, 2011. Robotics, Vision and Control, Springer Tracts in Advanced Robotics, Springer Berlin Heidelberg, Berlin, Heidelberg. http://dx.doi.org/10.1007/978-3-642-20144-8.

Coviello V, Arattano M, Comiti F, Macconi P, Marchi L, 2019. Seismic characterization of debris flows: Insights into energy radiation and implications for warning. Journal of Geophysical Research: Earth Surface,124, p. 1440 – 1463. https://doi.org/10.1029/2018JF004683.

Cui P, Guo X, Yan Y, Li Y, Ge Y, 2018. Real-time observation of an active debris flow watershed in the Wenchuan Earthquake area, Geomorphology, 321, p. 153 – 166. https://doi.org/10.1016/j.geomorph.2018.08.024.

Detert M, 2021. How to Avoid and Correct Biased Riverine Surface Image Velocimetry, Water Resources Research, 57(2). https://doi.org/10.1029/2020WR027833.

642 Dramais G, Le Coz J, Camenen B, Hauet A, 2011. Advantages of a mobile LSPIV method for
643 measuring flood discharges and improving stage-discharge curves. Journal of Hydro-environment
644 Research, 5(4), p. 301 – 312. https://doi.org/10.1016/j.jher.2010.12.005.

645 Elsinga GE, Van Oudheusden BW, Scarano F, 2005. The effect of particle image blur on the
646 correlation map and velocity measurement in PIV, Optical Diagnostics, International Society for
647 Optics and Photonics, 5880, p. 291 – 302. https://doi.org/10.1117/12.616572.

648 Eu S, Im S, Kim D, Chun KW, 2017. Flow and deposition characteristics of sediment mixture in
649 debris flow flume experiments. Forest Science and Technology, 13(2), p. 61 – 65.
650 https://doi.org/10.1080/21580103.2017.1311949.

651 Faug T, Childs P, Wyburn E, Einav I, 2015. Standing jumps in shallow granular flows down smooth
652 inclines, Physics of Fluids, 27(7), p. 22. https://doi.org/10.1063/1.4927447.

653 Fujita I, Muste M, Kruger A, 1998. Large-scale particle image velocimetry for flow analysis in
654 hydraulic engineering applications, Journal of Hydraulic Research, 36(3), 397 – 414.
655 https://doi.org/10.1080/00221689809498626.

656 Fujita I, Kunita Y, 2011. Application of aerial LSPIV to the 2002 flood of the Yodo River using a
657 helicopter mounted high density video camera, Journal of Hydro-environment Research, 5(4), p. 323
658 – 331. https://doi.org/10.1016/j.jher.2011.05.003.

659 Gollin D, Brevis W, Bowman ET, Shepley P, 2017. Performance of PIV and PTV for granular flow
660 measurements. Granular Matter 19(3), 42. https://doi.org/10.1007/s10035-017-0730-9.

661 Gunawan B, Sun X, Sterling M, Shiono K, Tsubaki R, Rameshwaran P, Knight DW, Chandler JH,
662 Tang X, Fujita I, 2012. The application of LS-PIV to a small irregular river for inbank and overbank
663 flows, Flow Measurement and Instrumentation 24, p. 1 – 12.
664 http://dx.doi.org/10.1016/j.flowmeasinst.2012.02.001.

665 Hosseini MS, Plataniotis KN, 2020. Convolutional Deblurring for Natural Imaging, IEEE
666 Transactions on Image Processing, 29, p. 250 – 264. https://doi.org/10.1109/TIP.2019.2929865.

667 Hürlimann M, Rickenmann D, Graf C, 2003. Field and monitoring data of debris-flow events in the
668 Swiss Alps, Canadian Geotechnical Journal, 40(1), p. 161 – 175. https://doi.org/10.1139/t02-087.

669 Hürlimann M, Coviello V, Bel C, Guo X, Berti M, Graf C, Hübl J, Miyata S, Smith JB, Yin Hy,
670 2019. Debris-flow monitoring and warning: Review and examples, Earth-Science Reviews, 199.
671 https://doi.org/10.1016/j.earscirev.2019.102981.

672 Iverson RM, Logan M, LaHusen RG, Berti M, 2010. The perfect debris flow? Aggregated results
673 from 28 large-scale experiments, Journal of Geophysical Research: Earth Surface, 115, F03005.
674 https://doi.org/10.1029/2009JF001514.

675 Iverson RM, 2015. Scaling and design of landslide and debris-flow experiments, Geomorphology,
676 244, p. 9 – 20. https://doi.org/10.1016/j.geomorph.2015.02.033.

677 Jolley MJ, Russell AJ, Quinn PF, Perks MT, 2021. Considerations when applying Large-Scale PIV
678 and PTV for determining river flow velocity. Frontiers in Water, 3.
679 https://doi.org/10.3389/frwa.2021.709269.

680 Jop P, 2015. Rheological properties of dense granular flows, Comptes Rendus Physique 16(1), p. 62
681 – 72. https://doi:10.1016/j.crhy.2014.12.001.

Jop P, Forterre Y, Pouliquen O, 2005. Crucial role of sidewalls in granular surface flows: Consequences for the rheology, Journal of Fluid Mechanics 541, p. 167 – 192. https://doi:10.1017/S0022112005005987.

Jop P, Forterre Y, Pouliquen O, 2006. A constitutive law for dense granular flows, Nature 441(7094), p. 727 – 730. https://doi.org/10.1038/nature04801.

Kaitna R, Palucis MC, Yohannes B, Hill KM, Dietrich WE, 2016. Effects of coarse grain size distribution and fine particle content on pore fluid pressure and shear behavior in experimental debris flows, Journal of Geophysical Research: Earth Surface, 121, p. 415 – 441. https://doi.org/10.1002/2015JF003725.

Kreizer M, Ratner D, Liberzon A, 2010. Real-time image processing for particle tracking velocimetry, Experiments in Fluids, 48, p. 105 – 110. https://doi.org/10.1007/s00348-009-0715-5.

Le Boursicaud R, Pénard L, Hauet A, Thollet F, Le Coz J, 2016. Gauging extreme floods on YouTube: application of LSPIV to home movies for the post-event determination of stream discharges, Hydrological Processes, 30(1), p. 90 – 105. https://doi.org/10.1002/hyp.10532.

Le Coz J, Hauet A, Pierrefeu G, Dramais G, Camenen B, 2010. Performance of image-based velocimetry (LSPIV) applied to flash-flood discharge measurements in Mediterranean rivers, Journal of Hydrology, 394, p. 42 – 52. https://doi.org/10.1016/j.jhydrol.2010.05.049.

Le Coz J, Renard B, Vansuyt V, Jodeau M, Hauet A, 2021. Estimating the uncertainty of video-based flow velocity and discharge measurements due to the conversion of field to image coordinates. Hydrological Processes, 35(5). https://doi.org/10.1002/hyp.14169.

Leng Xp, Liu Dl, Wie Fq, Hong Y, Dai Df, 2017. Debris flows monitoring and localization using infrasonic signals, Journal of Mountain Science, 14(7) p. 1279 – 1291. https://doi.org/10.1007/s11629-016-3836-3.

Li K, Wang Y, Cheng Q, Lin Q, Wu Y, Long Y, 2022. Insight into granular flow dynamics relying on basal stress measurements: From experimental flume tests, Journal of Geophysical Research: Solid Earth, 127. https://doi.org/10.1029/2021JB022905.

Li W, Liao Q, Ran Q, 2019. Stereo-imaging LSPIV (SI-LSPIV) for 3D water surface reconstruction and discharge measurement in mountain river flows, Journal of Hydrology, 578. https://doi.org/10.1016/j.jhydrol.2019.124099.

Lian Z, Wang H, 2023. An image deblurring method using improved U-Net model based on multilayer fusion and attention mechanism. Scientific Reports 13(1), 21402. https://doi.org/10.1038/s41598-023-47768-4.

Lindken R, Rossi M, Grosse S, Westerweel J, 2009. Micro-Particle Image Velocimetry (PIV): Recent developments, applications, and guidelines, Lab on a Chip, 9(17), p. 2551 – 2567. https://doi.org/10.1039/b906558j.

Lucy LB, 1974. An iterative technique for the rectification of observed distributions, Astronomical Journal, 79, p. 745. https://doi.org/10.1086/111605.

Mainsant G, Larose E, Bronnima C, Jongmans D, Michoud C, Jaboyedoff M, 2012. Ambient seismic noise monitoring of a clay landslide: toward failure prediction. Journal of Geophysical Research: Earth Surface, 117, p. 1 – 12. https://doi.org/10.1029/2011JF002159.

Marr D, Hildreth E, 1980. Theory of Edge Detection, Proceedings of the Royal Society, 207, p. 187 – 217. https://royalsocietypublishing.org/doi/abs/10.1098/rspb.1980.0020.

McArdell BW, Bartelt P, Kowalski J, 2007. Field observations of basal forces and fluid pore pressure in a debris flow, Geophysical Research Letters, 34(7). https://doi.org/10.1029/2006GL029183.

Meyrat G, McArdell B, Ivanova K, Müller C, Bartelt P, 2022. A dilatant, two-layer debris flow model validated by flow density measurements at the Swiss illgraben test site, Landslides 19(2), p. 265 – 276. https://doi.org/10.1007/s10346-021-01733-2.

MiDi GDR, 2004. On dense granular flows, The European Physical Journal E, 14(4), p. 341 – 365. https://doi.org/10.1140/epje/i2003-10153-0.

Muste M, Fujita I, Hauet A, 2008. Large-scale particle image velocimetry for measurements in riverine environments, Water Resources Research, 44(4). https://doi.org/10.1029/2008WR006950.

Muste M, Hauet A, Fujita I, Legout C, Ho HC, 2014. Capabilities of large-scale particle image velocimetry to characterize shallow free-surface flows, Advances in Water Resources, 70, p. 160 – 171. https://doi.org/10.1016/j.advwatres.2014.04.004.

Nagl G, Hübl J, Kaitna R, 2020. Velocity profiles and basal stresses in natural debris flows. Earth Surface Processes and Landforms 45, p. 1764 – 1776. https://doi.org/10.1002/esp.4844.

Parsons JD, Whipple KX, Simoni A, 2001. Experimental Study of the Grain-Flow, Fluid-Mud Transition in Debris Flows, The Journal of Geology, 109(4), p. 427-447. https://doi.org/10.1086/320798.

Patalano A, García CM, Rodríguez A, 2017. Rectification of Image Velocity Results (RIVeR): A simple and user-friendly toolbox for large-scale water surface Particle Image Velocimetry (PIV) and Particle Tracking Velocimetry (PTV), Computers & Geosciences, 109, p. 323 – 330. https://doi.org/10.1016/j.cageo.2017.07.009.

Picarelli L, Urciuoli G, Ramondini M, Comegna L, 2005. Main features of mudslides in tectonised highly fissured clay shales, Landslides 2(1), p. 15 – 30. https://doi.org/10.1007/s10346-004-0040-2.

Prasad AK, Adrian RJ, Landreth CC, Offutt PW, 1992. Effect of resolution on the speed and accuracy of particle image velocimetry interrogation. Experiments in Fluids 13, p. 105 – 116. https://doi.org/10.1007/BF00218156.

Raffel M, Willert C, Wereley S, Kompenhans J, 2007. Particle Image Velocimetry, 2nd Edition, Springer Berlin, Heidelberg. https://doi.org/10.1007/978-3-540-72308-0.

Savage SB, 1979. Gravity flow of cohesionless granular materials in chutes and channels, Journal of Fluid Mechanics, 92(1), p. 53 – 96. https://doi:10.1017/S0022112079000525.

Satish P, Srikantaswamy M, Ramaswamy NK, 2020. A comprehensive review of blind deconvolution techniques for image deblurring. Traitement du Signal, 37(3), pp. 527 – 539. https://doi.org/10.18280/ts.370321.

Schöffl T, Nagl G, Koschuch R, Schreiber H, Hübl J, Kaitna R, 2023. A perspective of surge dynamics in natural debris flows through pulse-Doppler radar observations. Journal of Geophysical Research: Earth Surface, 128. https://doi.org/10.1029/2023JF007171.

Shapiro LG, Stockman GC, 2001. Computer Vision, Prentice Hall PTR, Upper Saddle River, NJ, USA. ISBN: 0130307963.

Spielmann R, Aaron J, 2024. A new method for detailed discharge and volume measurements of debris flows based on high-frequency 3D LiDAR point clouds; Illgraben, Switzerland, Engineering Geology, 329. https://doi.org/10.1016/j.enggeo.2023.107386.

Theule JI, Crema S, Marchi L, Cavalli M, Comiti F, 2018. Exploiting LSPIV to assess debris-flow velocities in the field, Natural Hazards and Earth System Sciences, 18, p. 1 – 13. https://nhess.copernicus.org/articles/18/1/2018/.

Thielicke W, 2014. The Flapping Flight of Birds – Analysis and Application, Ph.D. thesis Rijksuniversiteit Groningen. https://doi.org/10.13140/RG.2.2.18656.94728.

Thielicke W, Stamhuis E, 2014. Pivlab – towards user-friendly, affordable and accurate digital particle image velocimetry in MATLAB, Journal of Open Research Software, 2(1), 30. https://doi.org/10.5334/jors.bl.

Thielicke W, Sonntag R, 2021. Particle Image Velocimetry for MATLAB: Accuracy and enhanced algorithms in PIVlab. Journal of Open Research Software, 9(1), 12. https://doi.org/10.5334/jors.334.

Turnbull B, Bowman ET, McElwaine JN, 2015. Debris flows: Experiments and modelling, Comptes Rendus Physique, 16(1), p. 86 – 96. https://doi.org/10.1016/j.crhy.2014.11.006.

Vision Caltech, 2009. Camera Calibration Toolbox for Matlab. http://www.vision.caltech.edu/bouguetj/calib_doc/.

Walter F, Burtin A, McArdell BW, Hovius N, Weder B, Turowski JM, 2017. Testing seismic amplitude source location for fast debris-flow detection at Illgraben, Switzerland, Natural Hazards and Earth System Sciences, 17(6), p. 939 – 955. https://doi.org/10.5194/nhess-17-939-2017.

Wiederseiner S, Andreini N, Épely-Chauvin G, Moser G, Monnereau M, Gray JMNT, Ancey C, 2011. Experimental investigation into segregating granular flows down chutes, Physics of Fluids, 23(1). https://doi.org/10.1063/1.3536658.

Zanuttigh B, Lamberti A, 2007. Instability and surge development in debris flows, Reviews of Geophysics, 45(3). https://doi.org/10.1029/2005RG000175.

Zhang K, Zuo W, Gu S, Zhang L, 2017. Learning Deep CNN Denoiser Prior for Image Restoration, 2017 IEEE Conference on Computer Vision and Pattern Recognition (CVPR), Honolulu, HI, USA, p. 2808-2817, https://doi.org/10.1109/CVPR.2017.300.

Zhao Y, Take WA, Kaitna R, McArdell BW, McElwaine JM, Bowman ET, 2023. Fluid effects in model granular flows, Granular Matter 26(2). https://doi.org/10.1007/s10035-023-01365-4.

Zhu X, Lipeme Kouyi G, 2019. An analysis of LSPIV-based surface velocity measurement techniques for stormwater detention basin management, Water Resources Research, 55(2), p. 888 – 903. https://doi.org/10.1029/2018WR023813.

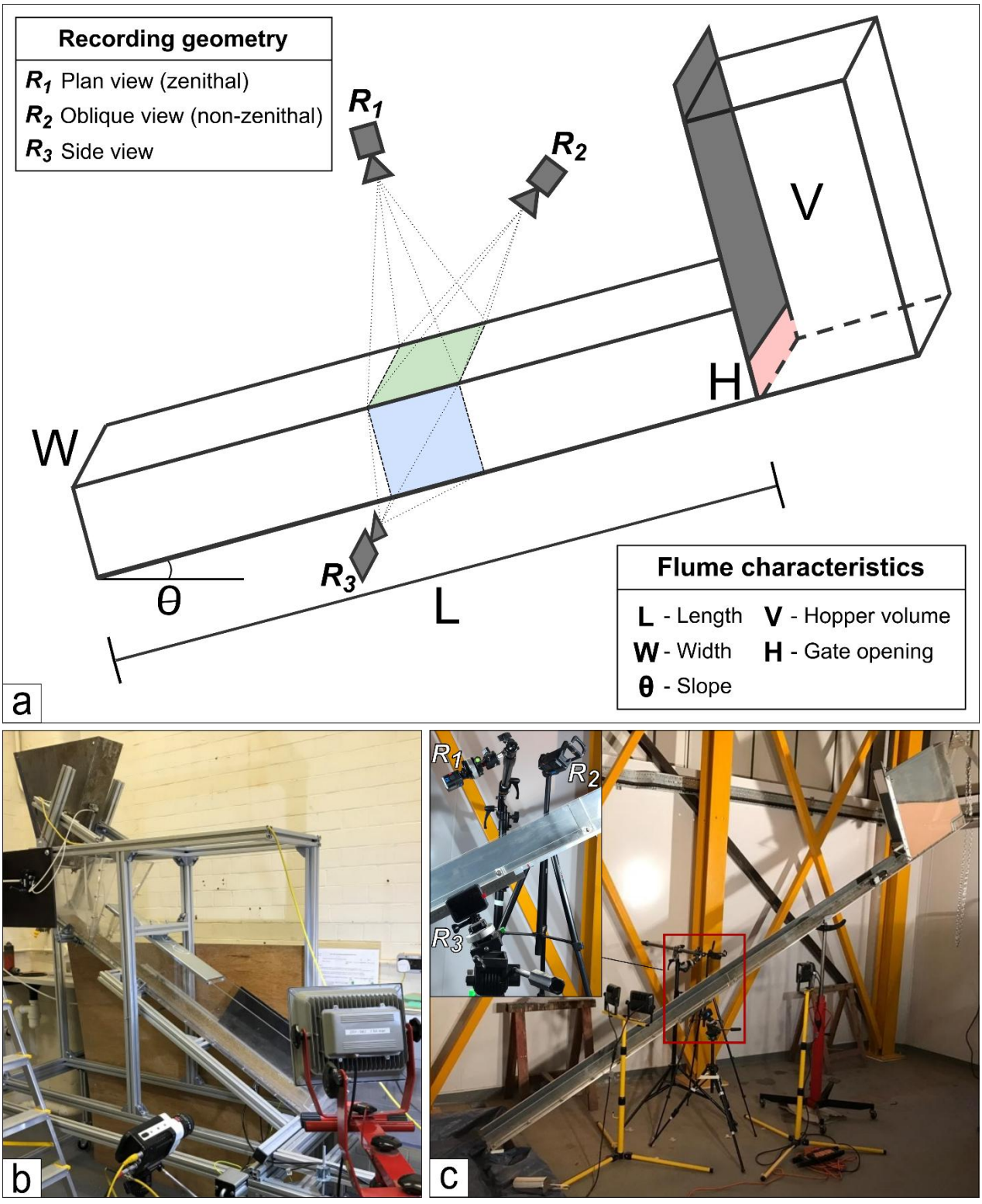

Fig. 1 – Experimental setup scheme (a) and pictures of the different laboratory equipment employed for *F1* (b) and *F2* (c) flume test sets.

Experimental setup	*F1*	*F2*
Flume length (*L*)	1.2 m	4 m
Flume width (*W*)	0.1 m	0.1 m
Flume slope (θ)	30°	0 – 33°
Hopper volume (*V*)	0.021 m³	0.05 m³
Gate opening (*H*)	0.085 m	0.04 m
Chute surface	- Smooth (aluminium) - Ceramic beads ($d \approx 1$ mm) - Angular sand ($d \approx 1 – 2$ mm)	Smooth (aluminium)
Material employed	Denstone® ceramic beads ($d_{mean} \approx 3.85$ mm)	Fine sand ($d_{mean} \approx 0.28$ mm)
Material volume	0.008 m³	0.03 m³
Cameras	*Phantom Miro M310* (Frame rate = 1000 fps)	*GoPro Hero 10 [R_1, R_3] – 11 [R_2]* (Frame rate = 240 fps)
Recording geometries	R_1, R_3	R_1, R_2, R_3
Recording Distances	- R_1 = 0.45 m - R_3 = 0.40 m	- R_1 = 0.25 m - R_2 = 0.30 m - R_3 = 0.20 m

Table 1 – Summary of the primary characteristics of the flume apparatus, granular material, cameras and recording geometries utilised in the *F1* (blue) and *F2* (orange) experiment sets.

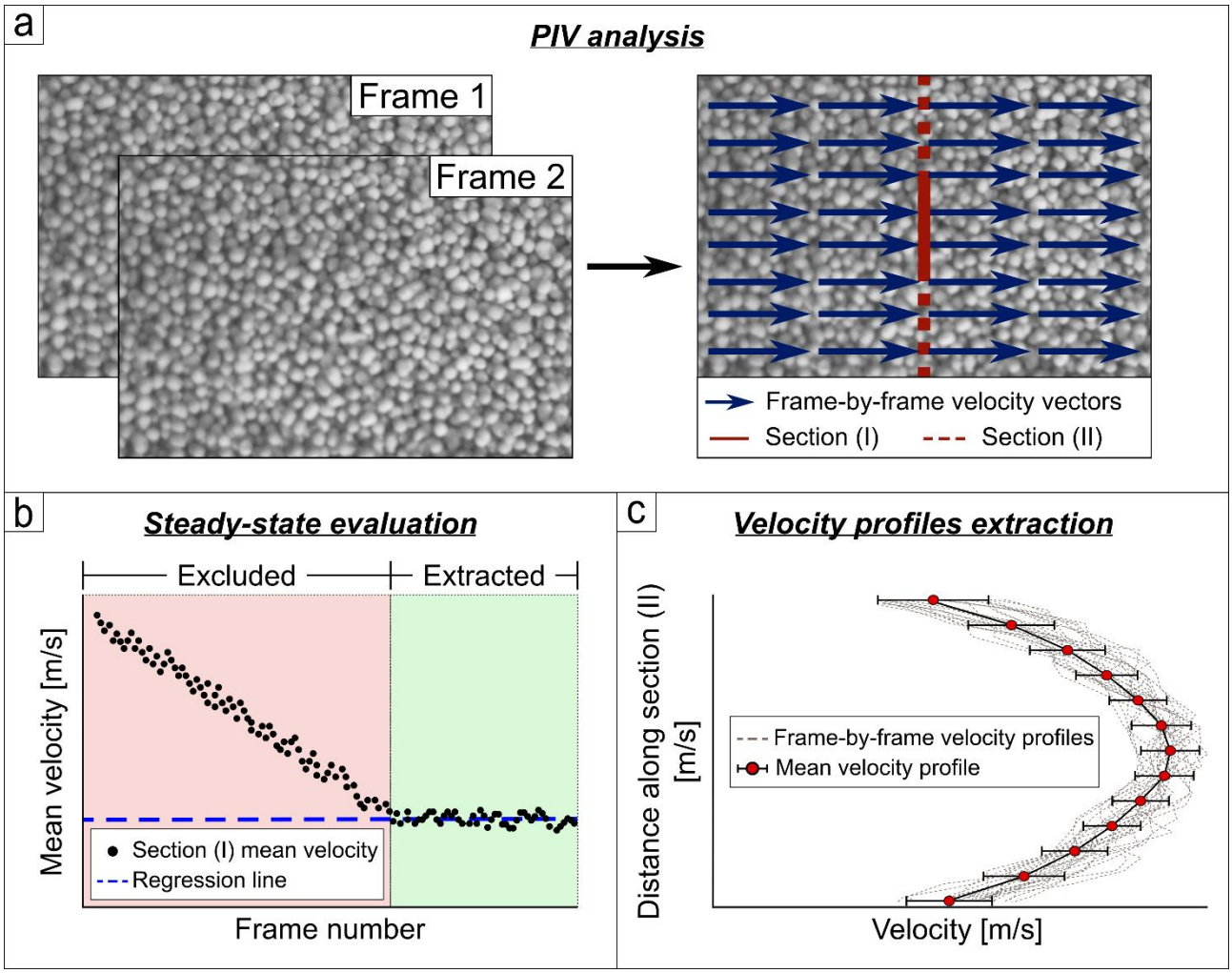

Fig. 2 – Summary of the processing chain employed to reconstruct the velocity profiles of the recorded flows, including determination of the flow velocity vectors through *PIV* (a), evaluation of the quasi-steady-state of the flow (b), and extraction of the velocity profiles for the identified steady-state frames subset along reference sections (c).

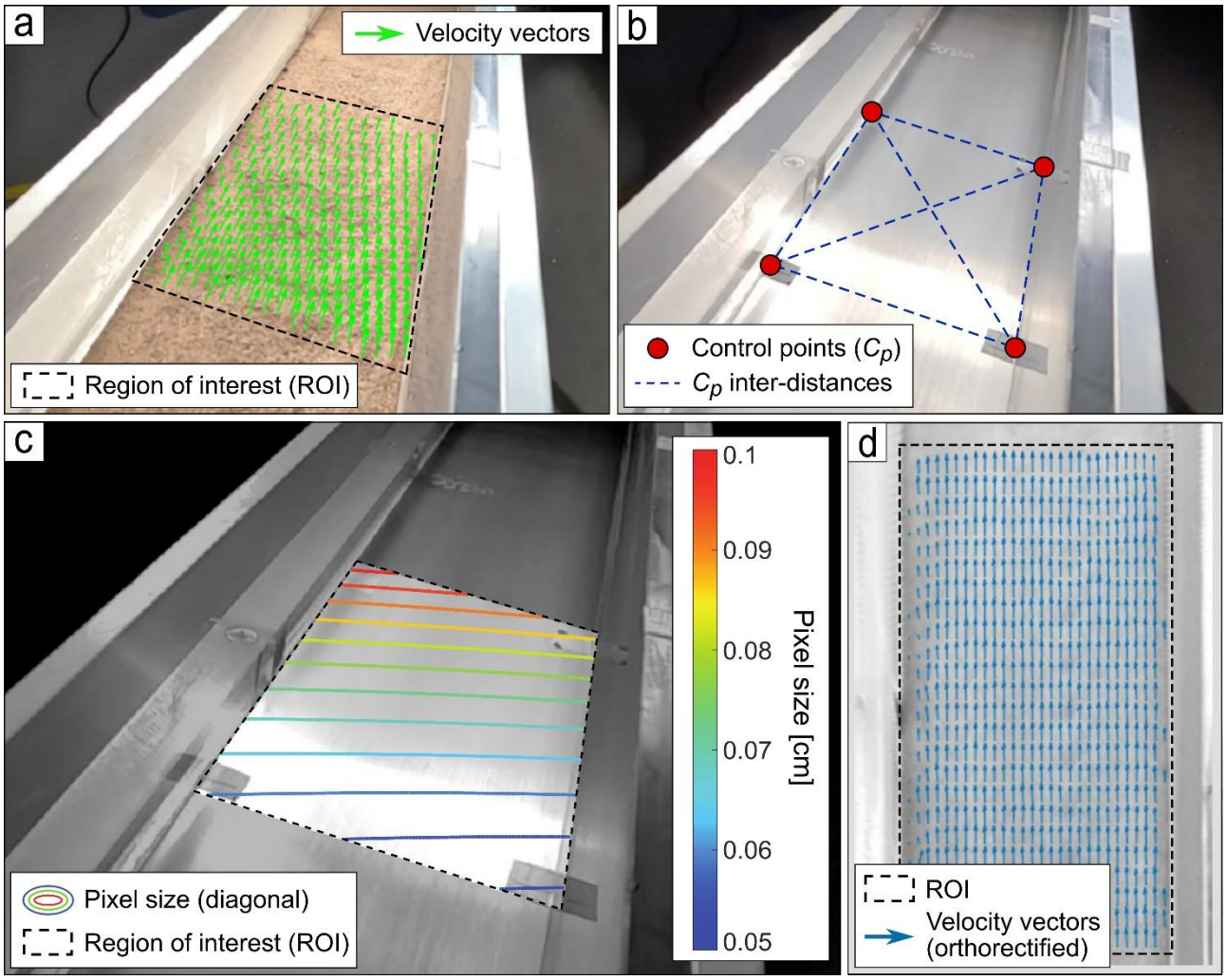

Fig. 3 – Camera perspective and example of the distorted *PIV*-derived flow velocity filed from R_2 recording geometry in *F2* flume tests (a). Locations of the four control points on the flume chute (b) required for applying the orthorectification algorithm in *RIVeR* (Patalano et al. 2017) to mitigate distortions from non-zenithal acquisitions by calculating the distribution of the actual pixel sizes across the image (c) and reprojecting the flow velocity vectors as if observed from a zenithal perspective (d).

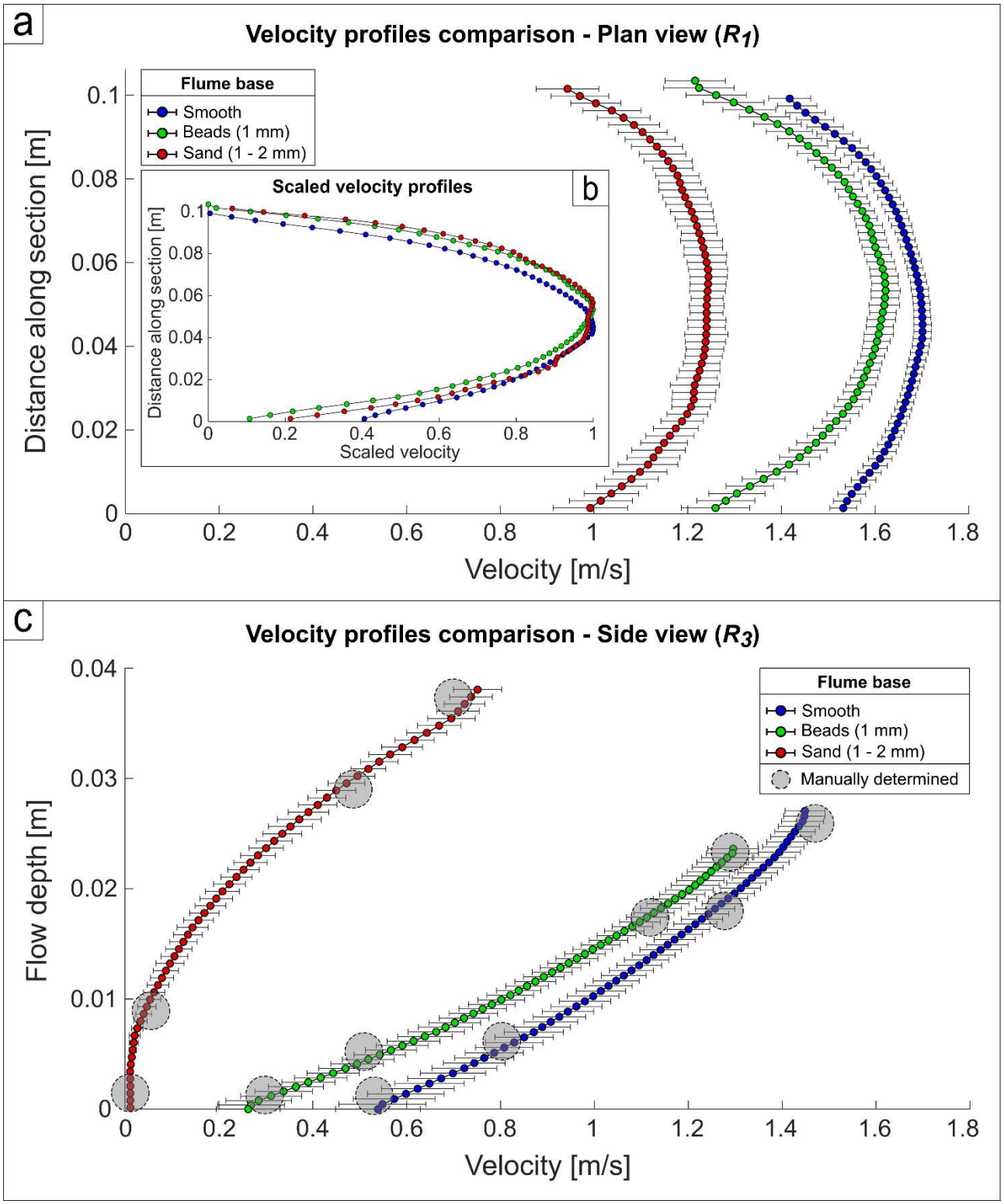

Fig. 4 – Surface velocity distributions, both original (a) and normalised (b), along with side velocity profiles (c) relative to the flows recorded in the *F1* flume experiments set. The velocity distributions are colour-coded based on the boundary conditions imposed at the base of the flow, achieved by varying its roughness: smooth (blue), intermediate (green, constituted of 1mm ceramic beads), and coarse sand (red). The grey circles in (b) indicate manually determined velocity values, with circle size corresponding to the diameter of visually tracked beads.

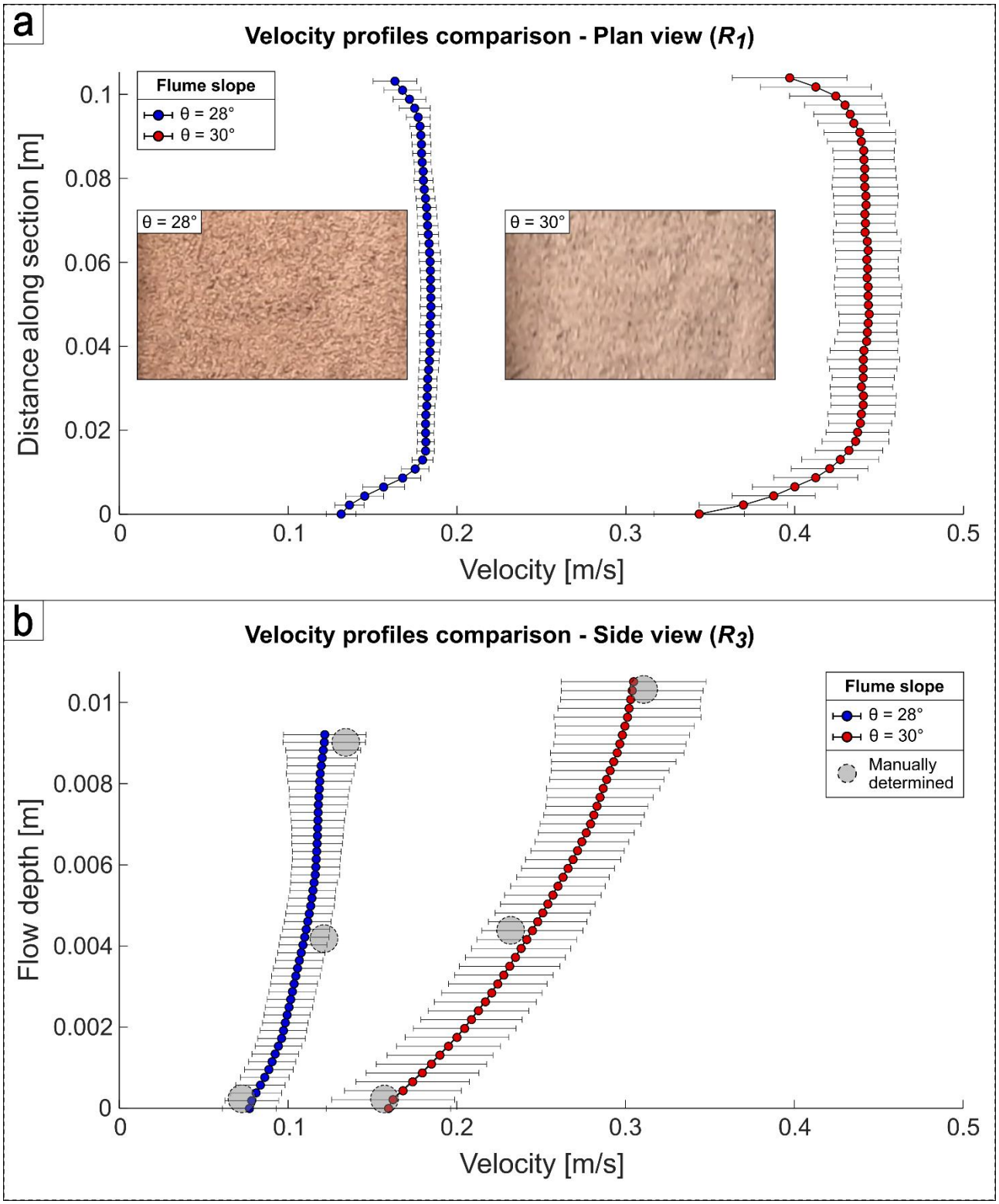

Fig. 5 – Surface (a) and side (b) velocity profiles for the flows captured in the *F2* flume experiments set. The velocity distributions are depicted in blue and red for the flows recorded at $\theta = 28°$ and $\theta = 30°$, respectively. Examples of plan view frames captured for the two image quality scenarios are also provided (a). The mild asymmetry in the surface velocity distributions in (a) may be attributed to a slight tilt in the flume chute. The grey circles in (b) indicate manually determined velocity values, with circle size corresponding to the diameter of visually tracked particles.

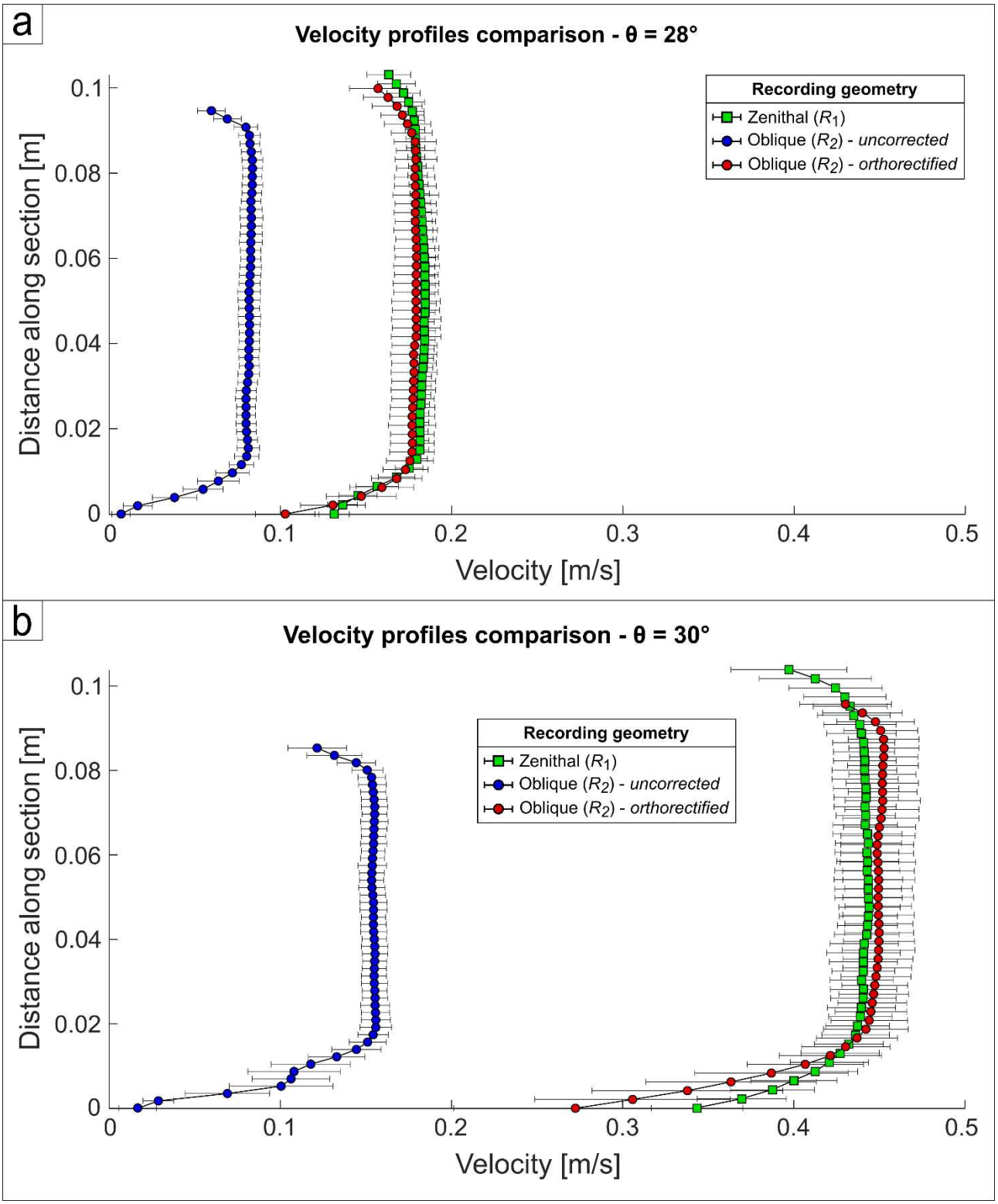

Fig. 6 – Comparison of the surface velocity distributions reconstructed along the same section from the R_1 perspective (green) and R_2 uncorrected (blue) and orthorectified (red) flow velocity fields, corresponding to two reference image quality scenarios of $\theta = 28°$ (a) and $\theta = 30°$ (b) considered in the *F2* experiments. The mild asymmetry in the surface velocity distributions in (a) may be attributed to a slight tilt in the flume chute.

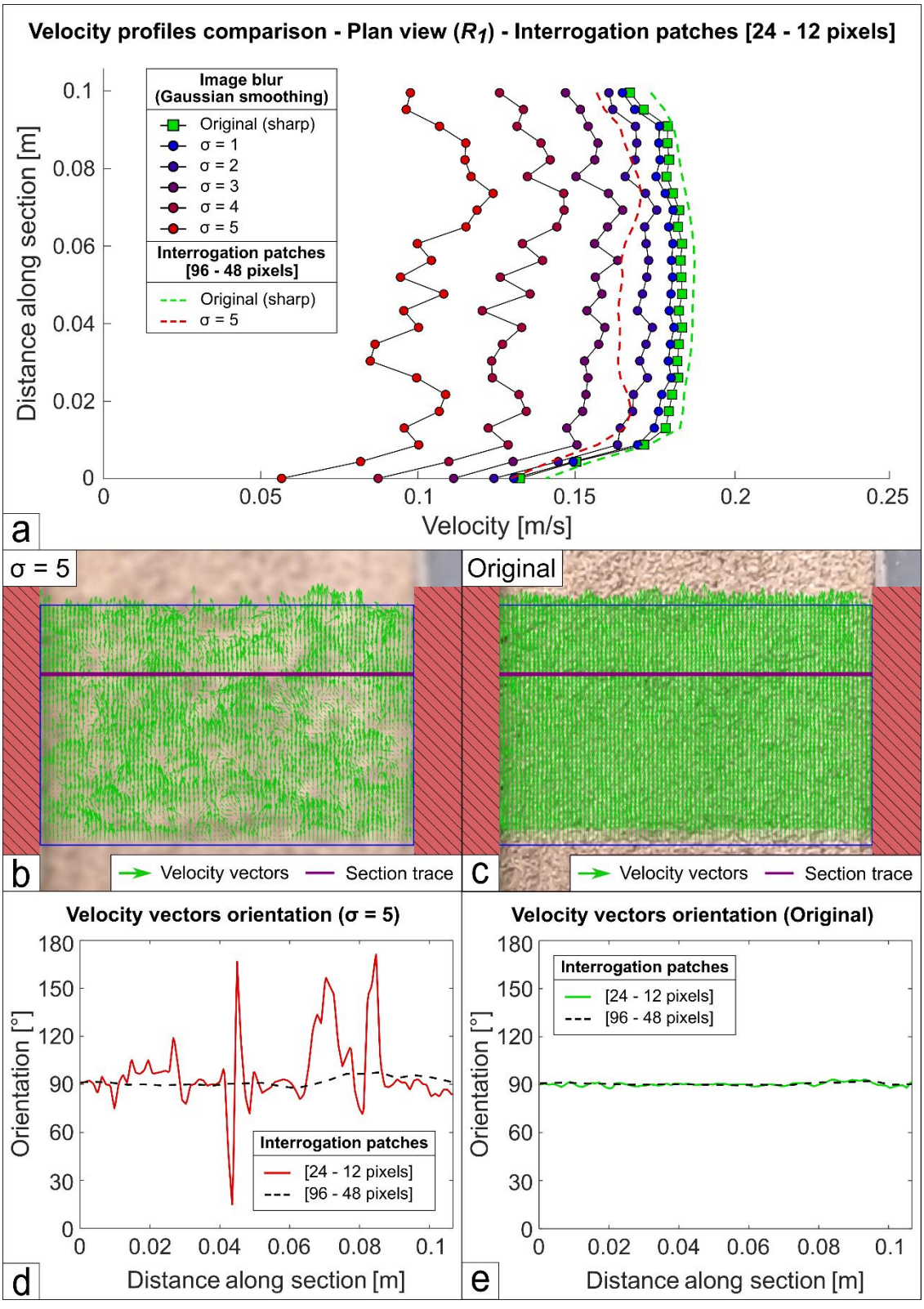

Fig. 7 – Surface velocity distributions reconstructed along a reference section from the R1 perspective using a sequence of moving interrogation patches of 24 – 12 pixels in the PIV analysis of the F2 test performed at θ = 28°. Curves are colour-coded based on the image blur level, expressed by the Gaussian smoothing filter parameter σ, increasing from blue to red. The green profile refers to the original sharp images. Dashed green and red lines represent the velocity profiles obtained from the real frames and highly blurred images ($\sigma = 5$), respectively, using an interrogation patch sequence of 96 – 48 pixels (a). Zenithal view of flow vectors reconstructed for the same frame pair analysed at $\sigma = 5$ (b) and for clear footage (c). Orientation of flow velocity vectors extracted along the purple line shown in (b) and (c) for highly blurred footage (d) and original images (e). The dashed black lines represent velocity vector orientations determined along the same section employing an interrogation patch sequence of 96 – 48 pixels in the *PIV* analysis.

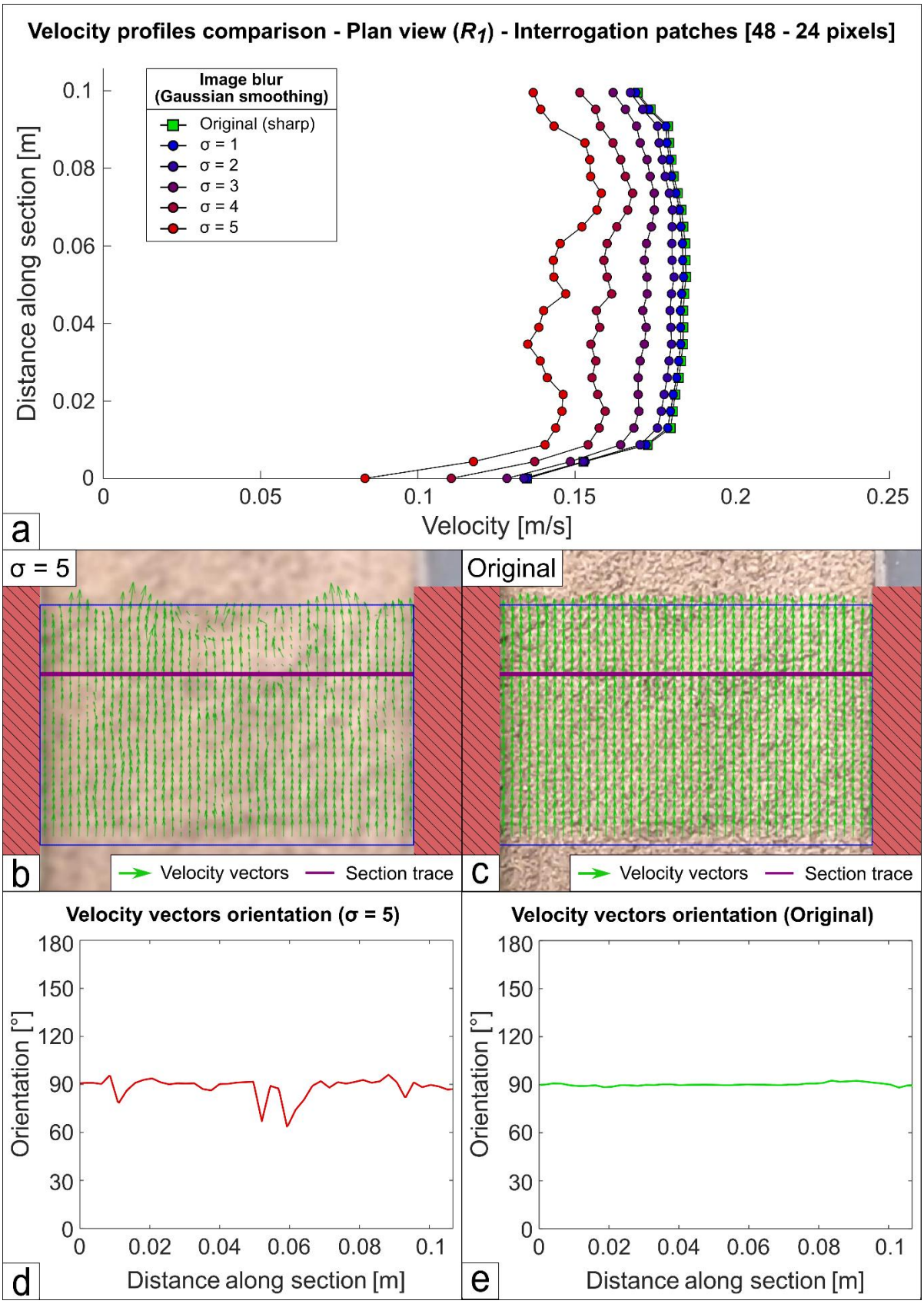

Fig. 8 – Surface velocity distributions reconstructed along a reference section from the R_1 perspective using a sequence of moving interrogation patches of 48 – 24 pixels in the PIV analysis of the *F2* test performed at $\theta = 28°$. Curves are colour-coded based on the image blur level, expressed by the Gaussian smoothing filter parameter σ, increasing from blue to red. The green profile refers to the original sharp images (a). Zenithal view of flow vectors reconstructed for the same frame pair analysed at $\sigma = 5$ (b) and for clear footage (c). Orientation of flow velocity vectors extracted along the purple line shown in (b) and (c) for highly blurred footage (d) and original images (e).

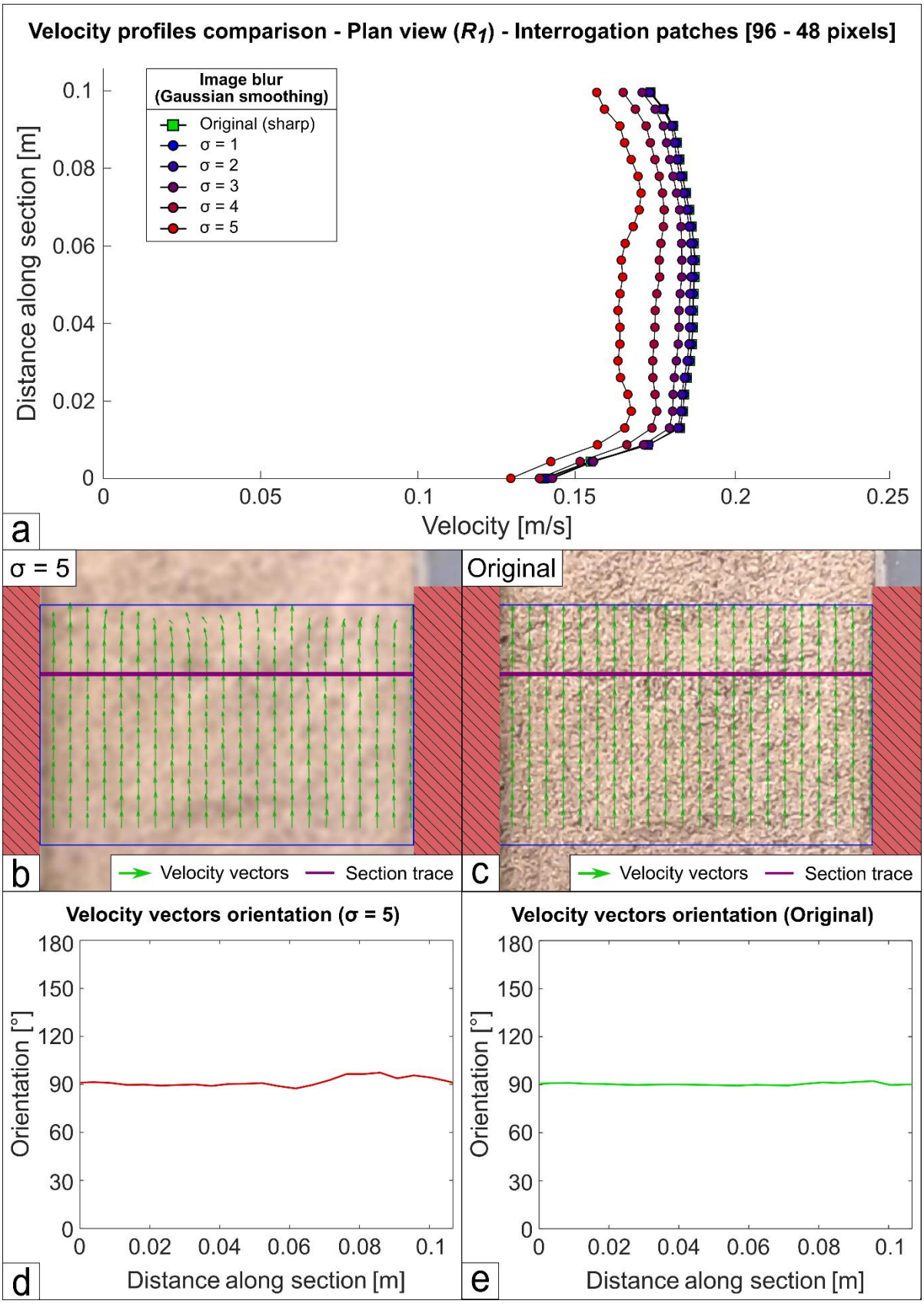

Fig. 9 – Surface velocity distributions reconstructed along a reference section from the R1 perspective using a sequence of moving interrogation patches of 96 – 48 pixels in the PIV analysis of the F2 test performed at θ = 28°. Curves are colour-coded based on the image blur level, expressed by the Gaussian smoothing filter parameter σ, increasing from blue to red. The green profile refers to the original sharp images (a). Zenithal view of flow vectors reconstructed for the same frame pair analysed at $\sigma = 5$ (b) and for clear footage (c). Orientation of flow velocity vectors extracted along the purple line shown in (b) and (c) for highly blurred footage (d) and original images (e).

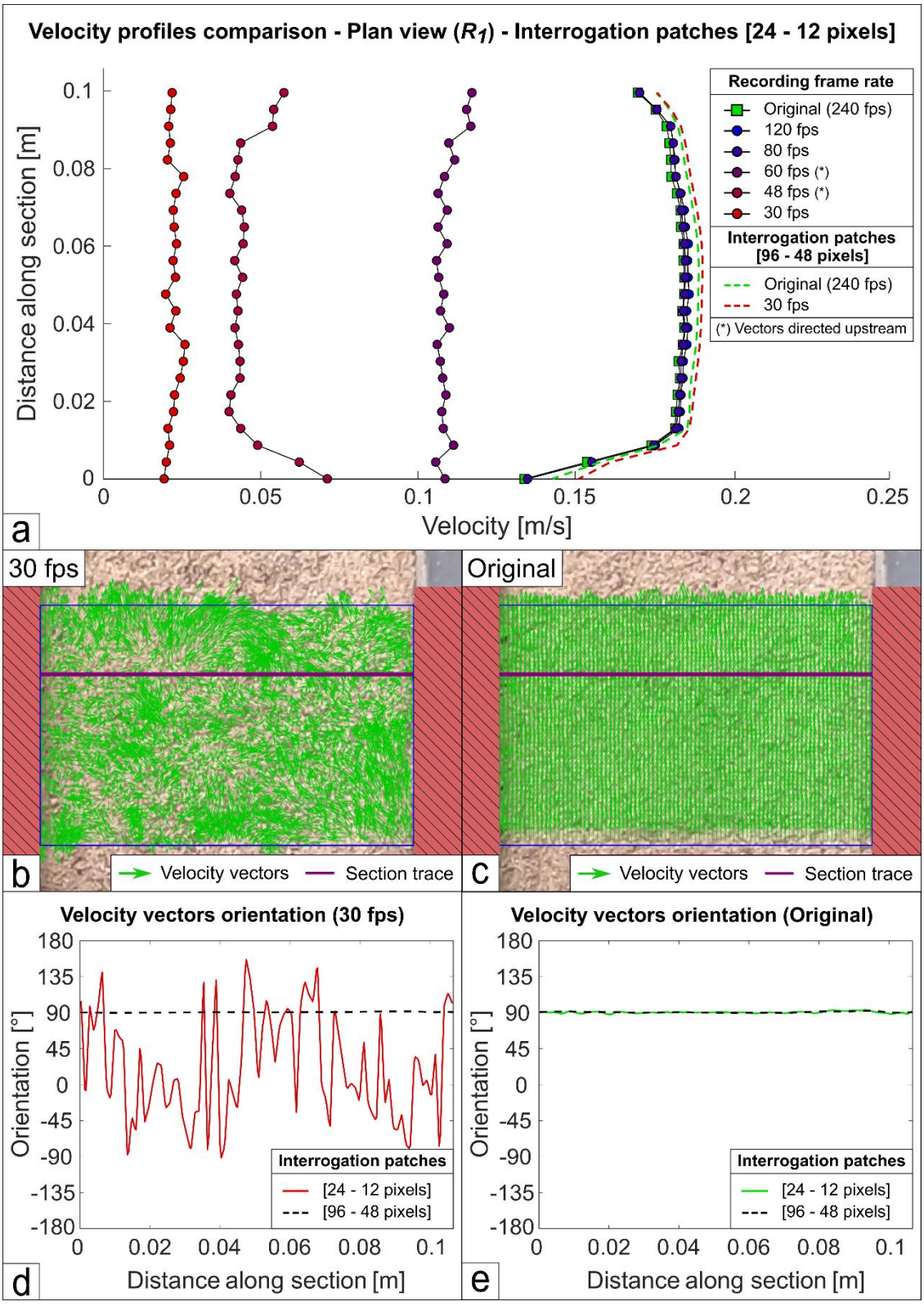

Fig. 10 – Surface velocity distributions reconstructed along a reference section from the R_1 perspective using a sequence of moving interrogation patches of 24 – 12 pixels in the PIV analysis of the *F2* test performed at $\theta = 28°$. Curves are colour-coded based on the recording frame rate, decreasing from blue to red. The green profile refers to the original images captured at 240 fps. Dashed green and red lines represent the velocity profiles obtained from the original images and footage undersampled at 30 fps, respectively, using an interrogation patch sequence of 96 – 48 pixels (a). Zenithal view of flow vectors reconstructed for the same frame pair analysed at 30 fps (b) and 240 fps footage (c). Orientation of flow velocity vectors extracted along the purple line shown in (b) and (c) for undersampled footage (d) and original images (e). The dashed black lines represent velocity vector orientations determined along the same section employing an interrogation patch sequence of 96 – 48 pixels in the *PIV* analysis.

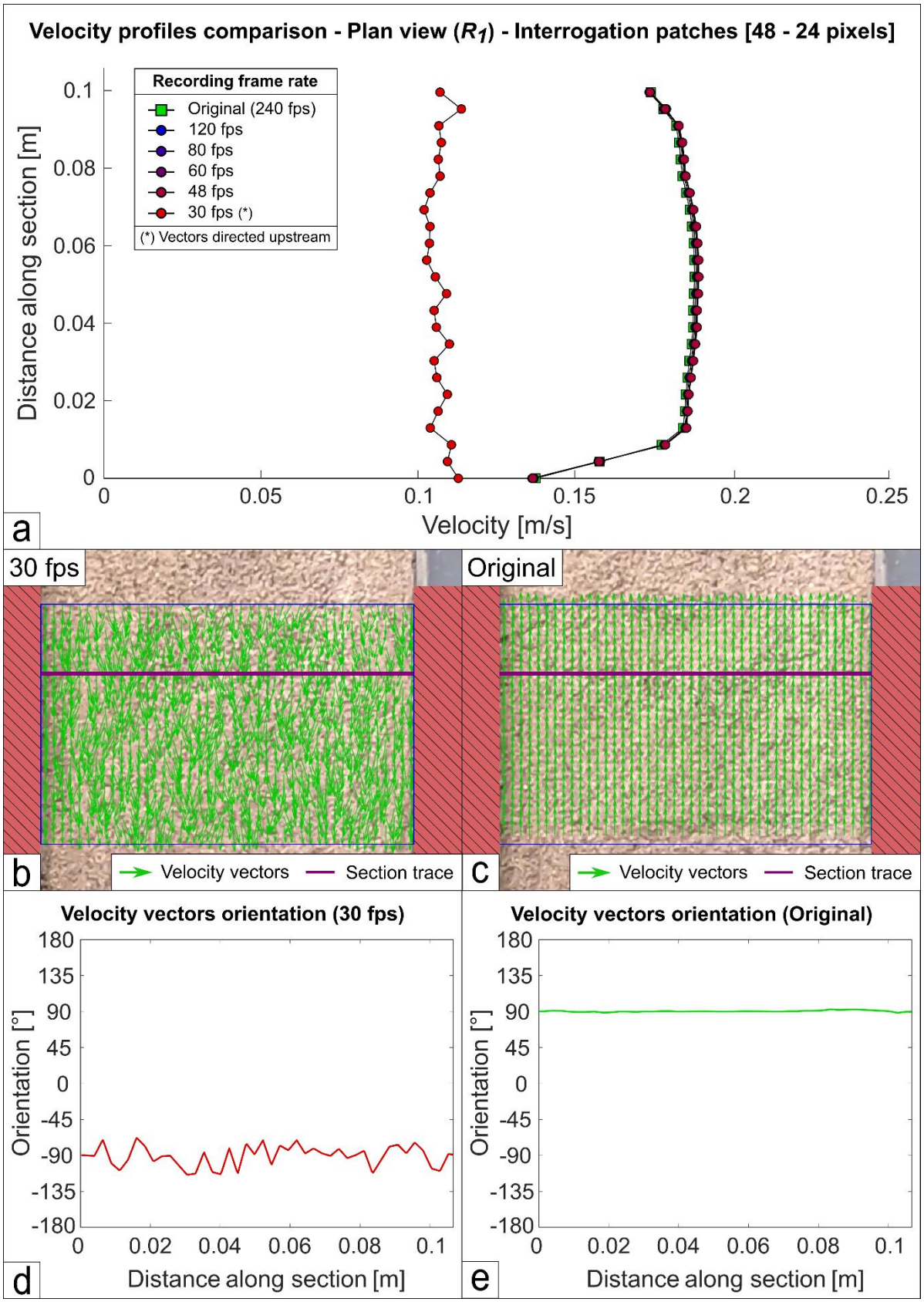

Fig. 11 – Surface velocity distributions reconstructed along a reference section from the R_1 perspective using a sequence of moving interrogation patches of 48 – 24 pixels in the PIV analysis of the *F2* test performed at $\theta = 28°$. Curves are colour-coded based on the recording frame rate, decreasing from blue to red. The green profile refers to the original images captured at 240 fps (a). Zenithal view of flow vectors reconstructed for the same frame pair analysed at 30 fps (b) and 240 fps footage (c). Orientation of flow velocity vectors extracted along the purple line shown in (b) and (c) for undersampled footage (d) and original images (e).

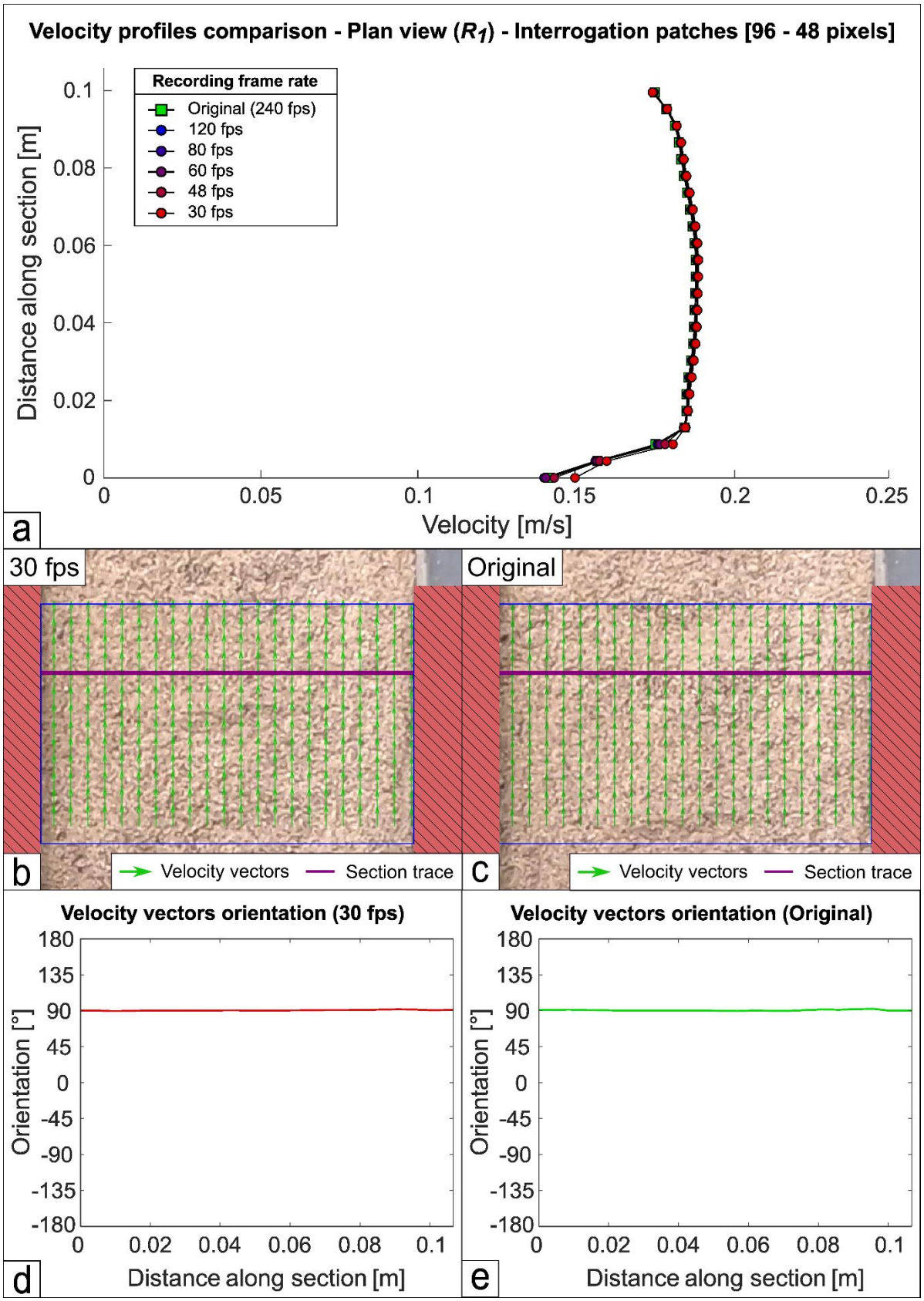

873

874 Fig. 12 – Surface velocity distributions reconstructed along a reference section from the R_1 perspective using a sequence
875 of moving interrogation patches of 96 – 48 pixels in the PIV analysis of the *F2* test performed at $\theta = 28°$. Curves are
876 colour-coded based on the recording frame rate, decreasing from blue to red. The green profile refers to the original
877 images captured at 240 fps (a). Zenithal view of flow vectors reconstructed for the same frame pair analysed at 30 fps (b)
878 and 240 fps footage (c). Orientation of flow velocity vectors extracted along the purple line shown in (b) and (c) for
879 undersampled footage (d) and original images (e).

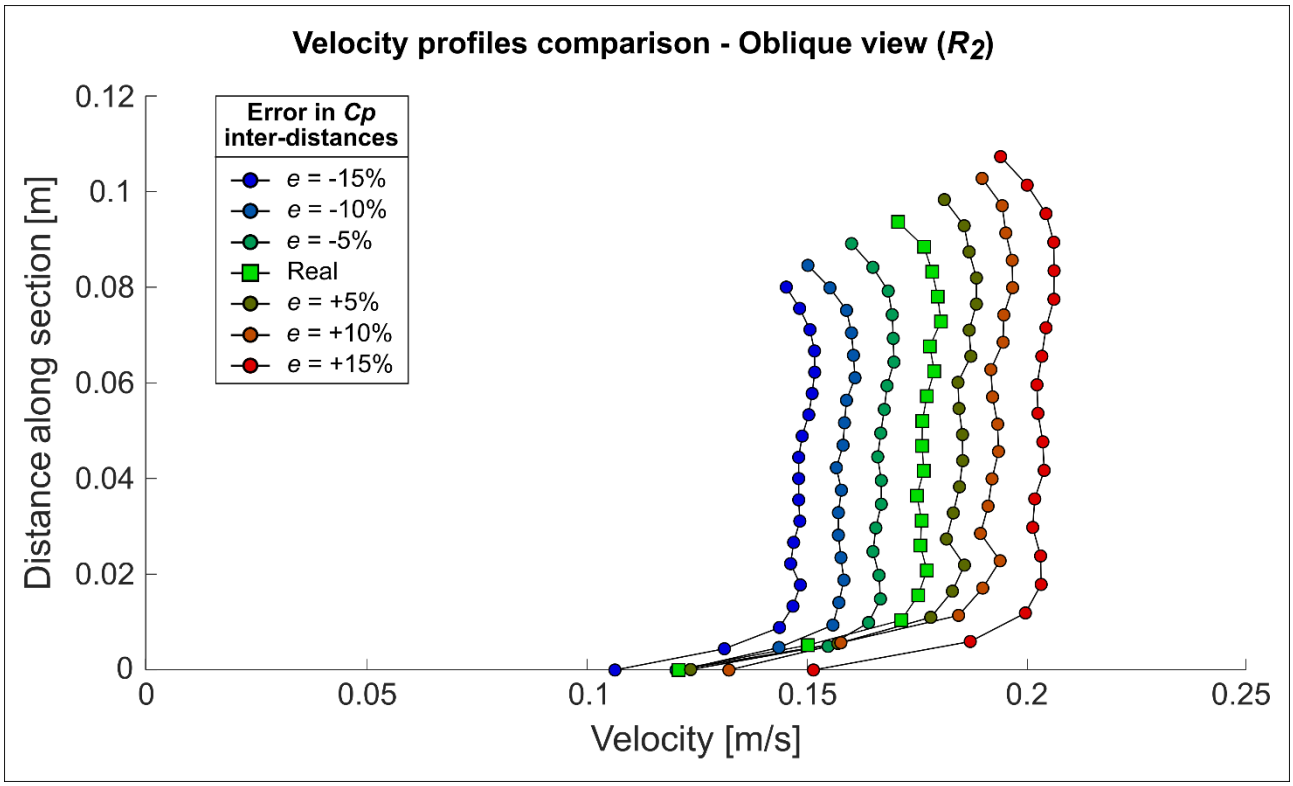

Fig. 13 – Comparison of the surface velocity distributions obtained from the orthorectified velocity fields from R_2 non-zenithal recordings of the *F2* test performed at $\theta = 28°$, assuming errors in the estimation of distances between control points of ± 5%, 10%, and 15% in the orthorectification procedure. The actual orthorectified velocity profile is shown in green. The curves grading towards red refer to overestimations, while those grading towards blue indicate underestimations.